

Electrosynthesis of Silane-Modified Magnetic Nanoparticles for Efficient Lead Ion Removal

Ayman E. Ahmed Elkholy,^[a] Kingsley Poon,^[b] Gurvinder Singh,^[b] Marcus Giansiracusa,^[c] Kimberley L. Callaghan,^[d] Colette Boskovic,^[c] Amanda V. Ellis,^[d] and Peter Kingshott*^[a, e]

The removal of heavy metal ions, such as lead (Pb^{2+}), from aqueous systems is critical due to their high toxicity and bioaccumulation in living organisms. This study presents a straightforward approach for the synthesis and surface modification of iron oxide nanoparticles (IONPs) for the magnetic removal of Pb^{2+} ions. IONPs were produced *via* electrosynthesis at varying voltages (10–40 V), with optimal magnetic properties achieved at 40 V resulting in highly crystalline and magnetic IONPs in the gamma-maghemite ($\gamma\text{-Fe}_2\text{O}_3$) phase. IONPs were characterized using various techniques including X-ray diffraction (XRD), Fourier transform infrared (FTIR) spectroscopy, vibrating sample magnetometry (VSM), transmission electron microscopy (TEM), and X-ray photoelectron spectroscopy (XPS).

A novel electrochemical method was developed for the silanization of IONPs using tetraethoxysilane (TEOS), (3-mercaptopropyl)trimethoxysilane (MPTMS) and (3-aminopropyl)triethoxysilane (APTES). The resulting silane-modified IONPs were evaluated for the magnetic removal of Pb^{2+} ions, with TEOS-modified IONPs demonstrating superior performance. This material exhibited a high adsorption capacity of 519 mg/g at a Pb^{2+} ion concentration of 300 ppm, and high removal efficiency across a range of Pb^{2+} ion concentrations, attributed to its $\text{Fe}_2\text{O}_3@\text{SiO}_2$ core-shell structure. This study highlights the potential of the electrochemical synthesis and silanization of nanoparticles for heavy metal remediation in water.

1. Introduction

The contamination of water resources by heavy metal ions is a critical environmental concern that poses significant risks to both human health and ecosystems.^[1–2] Several techniques have been widely used for the removal of water contaminants, such as chemical precipitation, ion exchange, and membrane separation.^[3] However, these methods often require high operational costs.^[4] On the other hand, using magnetic adsorbents has emerged as a simple and effective strategy to remove various water contaminants such as heavy metal ions^[1, 3] and organic dyes,^[5–6] with high efficiency and without generating secondary pollutants.^[5] Lead (Pb) in its ionic form (Pb^{2+}) is

particularly concerning amongst the hazardous heavy metals due to its high toxicity, persistence in the environment, and ability to bioaccumulate in living organisms.^[7] Pb^{2+} ion contamination in water can arise from various sources, including industrial processes,^[2] mining activities, and improper disposal of Pb-containing products.^[7] Even at low concentrations, Pb^{2+} ion exposure can cause severe health effects, including neurological damage,^[4] kidney dysfunction, bone deformations and mental disorders.^[1] As a result, there is an urgent need for effective and sustainable methods to remove Pb^{2+} ions from contaminated water.

Magnetic iron oxide nanoparticles (IONPs) have emerged as a promising class of materials for environmental remediation due to their unique properties. These nanoparticles offer high surface area-to-volume ratios, which enhance their adsorption capacity.^[3, 6] In addition, they have low toxicity,^[4] and their intrinsic magnetic properties allow for their easy separation using an external magnetic field.^[2–3] IONPs can be synthesized using various methods such as sol-gel method,^[8] microwave-assisted synthesis,^[3] thermal decomposition,^[9] hydrothermal method,^[10] co-precipitation,^[11] and electrochemical synthesis (electrodeposition).^[12–13] Furthermore, they can be formed in various phases, e.g., hematite ($\alpha\text{-Fe}_2\text{O}_3$),^[4] maghemite ($\gamma\text{-Fe}_2\text{O}_3$),^[14] and magnetite (Fe_3O_4).^[5] However, unmodified IONPs tend to form aggregates,^[1, 5] and experience low stability particularly in acidic media,^[2] which limits their performance towards heavy metal ion removal. To overcome these limitations and enhance their effectiveness, surface modification strategies are required. These include coating with materials like silicon dioxide (SiO_2) to improve their stability and hydrophilicity,^[1] or anchoring specific functional groups such as carboxylic acid (COOH),^[7] amine (NH_2)^[3] and thiol (SH)^[15] func-

[a] Department of Chemistry and Biotechnology, Swinburne University of Technology, Hawthorn, VIC, Australia

[b] School of Biomedical Engineering and Sydney Nano Institute, The University of Sydney, Sydney, NSW, Australia


[c] School of Chemistry, The University of Melbourne, Parkville, VIC, Australia


[d] Department of Chemical Engineering, The University of Melbourne, Parkville, VIC, Australia

[e] Australian Research Council (ARC) Training Centre in Surface Engineering for Advanced Materials (SEAM), Swinburne University of Technology, Hawthorn, VIC, Australia

Correspondence: Prof. Peter Kingshott, Department of Chemistry and Biotechnology, Swinburne University of Technology, Hawthorn 3122, VIC, Australia.

Email: pkingshott@swin.edu.au

 Supporting Information for this article is available on the WWW under <https://doi.org/10.1002/cssc.202402098>

 © 2025 The Author(s). ChemSusChem published by Wiley-VCH GmbH. This is an open access article under the terms of the Creative Commons Attribution Non-Commercial License, which permits use, distribution and reproduction in any medium, provided the original work is properly cited and is not used for commercial purposes.

tional groups that can form stable complexes with heavy metal ions. Various nanomaterials based on functionalized IONPs have been reported for the magnetic removal of Pb^{2+} ions from aqueous systems.^[2, 7, 15]

Silane coupling agents, also known as organosilanes, are a unique class of materials commonly used for the surface modification of metal oxide nanoparticles in a process known as silanization.^[16] This strategy involves the attachment of organosilane molecules to nanoparticle surface, thus introducing new functional groups on the surface of the nanoparticles to improve their properties.^[16–17] Surface modification of IONPs through silanization has proven to be an effective strategy for improving their adsorption capabilities. Among the various organosilane agents, tetraethoxysilane (TEOS),^[3, 6, 8] (3-mercaptopropyl)trimethoxysilane (MPTMS),^[15] and (3-aminopropyl)triethoxysilane (APTES)^[3, 7, 18] have been widely studied for their ability to enhance the adsorption properties of IONPs. The Stöber method is a well-known technique for synthesizing SiO_2 nanoparticles and coating various nanoparticles with SiO_2 coatings. In this method, TEOS is hydrolyzed and then condensed in an alcoholic solution in the presence of water and a catalyst, typically ammonia (NH_4OH).^[19] This method is frequently employed for the modification of IONPs to form $\text{Fe}_x\text{O}_y/\text{SiO}_2$ core-shell structures.^[1–3]

Among the methods used for the synthesis of IONPs, electrodeposition is considered a simple and straightforward method for the rapid synthesis of IONPs at room temperature using simple precursors. However, the produced materials are usually poorly crystalline due to the low synthesis temperature.^[20] In this study, we introduce an optimized electrochemical approach for synthesizing IONPs with high yield and enhanced structure, morphology, and magnetic properties. This was accomplished by synthesizing IONPs at a relatively high voltage (40 V) in a non-aqueous, ethanol-based electrolyte. This approach enabled the production of IONPs with improved properties facilitated by electrothermal annealing resulting from the heat generated by the Joule heating effect. Joule heating has emerged as a promising method for the synthesis of various functional nanomaterials with enhanced properties by passing an electric charge through the reaction medium, thereby generating heat.^[21–22] In addition, we present a novel electrochemical method for the straightforward silanization of IONPs using various organosilanes, including TEOS, MPTMS, and APTES. The electrochemical silanization method was designed to enable the rapid and direct silanization of IONPs, eliminating the need for pre-activation of nanoparticles or pre-hydrolysis of silanes, making the process more efficient and straightforward. This process was facilitated by the *in-situ* generation of hydroxide ions through the electrolysis of trace water in an ethanol-based electrolyte, which catalyzed the hydrolysis and condensation of the silanes. Furthermore, the silanization was promoted by the heat generated by the Joule heating effect. To the best of our knowledge, this approach is unique and has not been previously reported. Furthermore, the performance of these silane-functionalized IONPs was evaluated for the magnetic

removal of Pb^{2+} ions, which demonstrated superior performance, particularly the TEOS-modified IONPs.

2. Results and Discussion

2.1. Nanoparticle Synthesis and Characterization

Iron oxide nanoparticles (IONPs) were electrochemically synthesized in ethanol at different voltages (10–40 V). In the anodic half-reaction, Fe is oxidized to form Fe^{3+} ions (Eq. 1), while the cathodic half-reaction generates OH^- ions through the electrolysis of water (Eq. 2). Fe^{3+} and OH^- ions subsequently combine to form $\text{Fe}(\text{OH})_3$ (Eq. 3).^[20] $\text{Fe}(\text{OH})_3$ can then partially dehydrate to form hydrated amorphous Fe_2O_3 ($\text{Fe}_2\text{O}_3 \cdot n\text{H}_2\text{O}$) (Eq. 4), which can further transform into alpha-hematite ($\alpha\text{-Fe}_2\text{O}_3$) or gamma-maghemite ($\gamma\text{-Fe}_2\text{O}_3$) through further dehydration and crystallization.^[23] The amount of H_2O (~5%) included in the electrolyte was small to decrease the rate of IONP crystal growth and prevent their agglomeration into larger particles.^[12] In addition, the electrosynthesis process was conducted under stirring to keep the produced IONPs suspended in the electrolyte, and to prevent their adhesion to the cathode. Moreover, the sodium dodecyl sulfate (SDS) surfactant was used to help keep the IONPs suspended. The stirring was mild to reduce the dissipation of heat generated during the electrosynthesis, minimizing thermal energy loss to the surroundings. This optimized protocol aimed to make ultrasmall and uniform IONPs and to exploit the generated heat to improve their properties, as will be discussed further.

Anodic reaction:



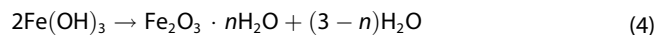
Cathodic reaction:



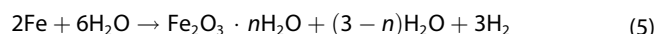
Ferric hydroxide formation:



Ferric hydroxide dehydration:



Overall reaction:



Figures 1(a) and 1(b) show the change in current and temperature, respectively, recorded during the electrosynthesis of IONPs. It was observed that the current remained steady around 59 mA during electrosynthesis at 10 V, with the temperature being nearly constant at around 20 °C. At 20 and 30 V, the current gradually and slowly increased over time, accompanied

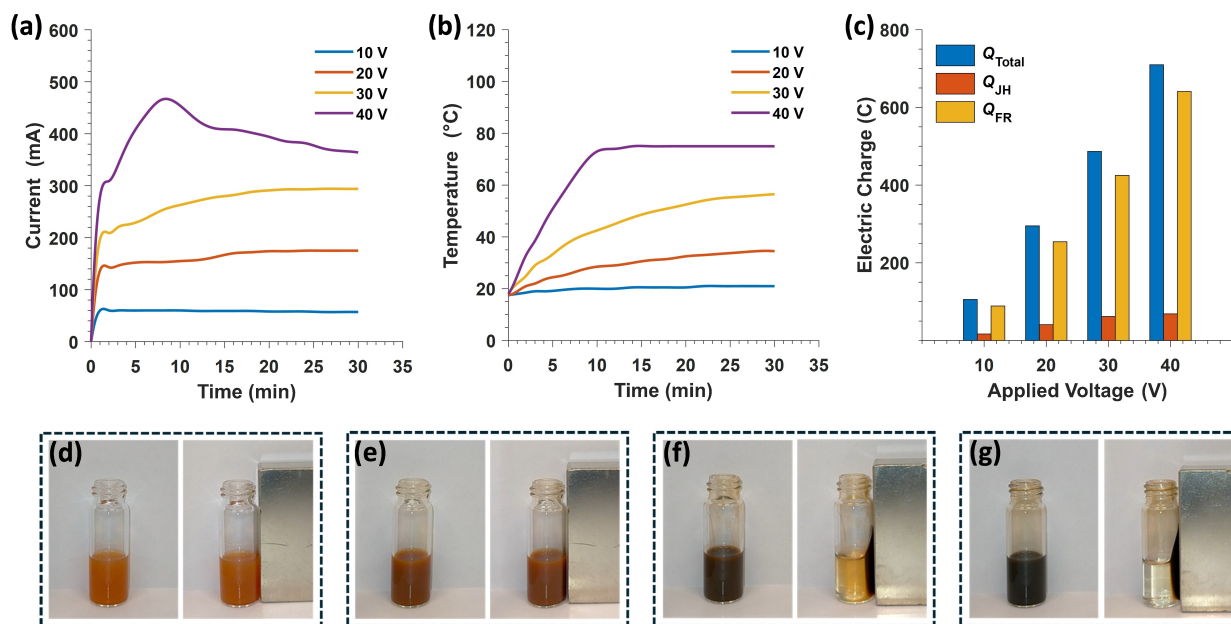


Figure 1. (a) Current and (b) temperature vs. time profiles recorded during the electrosynthesis of IONPs in an ethanol-based electrolyte at different voltages (10, 20, 30, and 40 V). (c) Total electric charge (Q_{Total}) calculated at different applied voltages and its components contributing to Joule heating (Q_{JH}), and Faradaic reaction (Q_{FR}). (d–g) Photographs of the magnetic response of IONP suspensions synthesized at voltages of (d) 10 V, (e) 20 V, (f) 30 V, and (g) 40 V – each pair shows the suspensions before (left) and after (right) applying a magnetic field using an Nd magnet for 2 min.

by a concurrent rise in temperature, reaching 34.5 °C and 56.5 °C after 30 min, respectively. In contrast, at 40 V, the current increased significantly, peaking at 467 mA within the first 10 min, accompanied by a sharp temperature rise to 73.4 °C. After this initial period, the current began to decrease slowly, while the temperature increased slightly and stabilized around 75 °C. The decrease in current was attributed to the partial evaporation of the ethanol-based electrolyte due to the high temperature, which is close to the boiling point of ethanol (78 °C), reducing the contact surface area between the Fe electrode and the electrolyte. The heating of the electrolyte during electrosynthesis occurred due to the passage of current through the electrolyte, resulting from its resistance, a phenomenon known as the Joule heating effect.^[24]

Figure 1(c) shows the total amount of electric charge (Q_{Total} , C) supplied to the electrosynthesis system at each applied voltage. These values were calculated by integrating the current vs. time profiles using Eq. 6.^[25–26]

$$Q = \int_0^t I \, dt \quad (6)$$

where I is the current (A) recorded during the electrosynthesis over a time period t (s). It can be seen that Q increases linearly as a function of the applied voltage. However, given that the electrolyte temperature increases during IONP electrosynthesis, the amount of charge supplied to the electrochemical cell was not fully consumed by Faradaic redox reactions (shown in Eq. 1 and Eq. 2). Therefore, it is essential to calculate the fraction of electric charge consumed in heating the system due to the Joule heating effect (Q_{JH}) and the fraction consumed by

Faradaic reactions (Q_{FR}). Both electric charge fractions were calculated as follows:

(a) The amount of heat energy (q_{JH} , J) generated by Joule heating effect at different applied voltages was calculated using Eq. 7^[27–28] based on the temperature vs. time profiles shown in Figure 1(b).

$$q_{\text{JH}} = mc \int_0^t T \, dt \quad (7)$$

where m is the mass of ethanol liquid (19.73 g), being the primary component of the electrolyte, while c is its specific heat capacity which is 2.44 J/g · °C.^[29] The q_{JH} values calculated at 10, 20, 30 and 40 V were 168.5, 818.2, 1853.0 and 2743.4 J, respectively.

(b) Assuming no heat dissipation to surroundings, the electrical energy consumed due to the Joule heating effect (W , J) is equivalent to the measured heat energy generated, i.e., $W = q_{\text{JH}}$. Therefore, Q_{JH} was calculated based on W values using the basic Joule's law of heating (Eq. 8).^[21, 30]

$$W = I^2 R t = QV \quad (8)$$

where I is the current (A), R is the resistance (Ω), t is the time (s) and V is the applied voltage (V). Subsequently, Q_{JH} was subtracted from Q_{Total} to give rise to Q_{FR} .

Table S1 shows that Q_{JH} values are 16.85, 40.91, 61.77 and 68.58 C at 10, 20, 30 and 40 V, respectively. In contrast, the corresponding Q_{FR} values were substantially higher at 88.87, 254.17, 424.89 and 641.16 C, respectively, demonstrating a semi-linear relationship with the applied voltage (Figure 1(c)). In

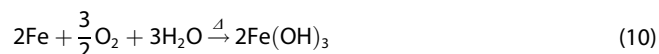
addition, at all applied voltages, most of the electric charge supplied to the electrosynthesis system ($87.0 \pm 2.6\%$) was consumed by the Faradaic redox reactions, i.e., $Q_{FR} \sim 0.87Q_{Total}$, whereas a small amount was converted into heat. The amount of IONPs electrodeposited *via* Faradaic reactions (m_{FR} , g) was calculated using Faraday's law, Eq. 9:^[31–32]

$$m_{FR} = \frac{Q_{FR}M}{nF} \quad (9)$$

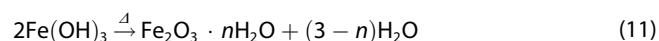
where M is the molecular mass of Fe_2O_3 (159.69 g/mol), n is the number of electrons transferred which is 6 for Fe_2O_3 electrodeposition by Fe oxidation according to Eq. 5, and F is Faraday's constant (96,485 C/mol). The term M/nF represents the electrochemical equivalent (Z , g/C),^[33–34] which is the proportionality constant. Therefore, Z relates the amount of IONPs deposited to the amount of electric charge passed through the electrolyte and consumed by Faradaic reactions (Q_{FR}), and it was calculated as 2.76×10^{-4} g/C.

Table S1 also shows that the amount of IONPs formed electrochemically *via* Faradaic redox reactions (m_{FR}), as described by Eq. 5, significantly increases with the applied voltage, reaching approximately 0.18 g at 40 V compared to approximately 0.03 g at 10 V. However, the experimentally obtained amounts at different voltages are higher than these calculated values. This means that a portion of the IONPs was produced by a non-electrochemical process, which is suggested to be *via* direct thermal oxidation of Fe to Fe_2O_3 using the dissolved oxygen in the electrolyte, as shown in Eqs. 10–12.

Ferric hydroxide formation:



Ferric hydroxide dehydration:



Overall reaction:



The amounts of thermally obtained IONPs due to Joule heating effect (m_{JH}) was calculated at different applied voltages (Table S1), which were found to be smaller than the electrochemically deposited amounts (m_{FR}) regardless of the applied voltage. However, m_{JH} values were found to be negligible at 10 V, but they increased significantly with the applied voltage reaching 0.07 g at 30 V. At 40 V, almost no increase was observed although the heat energy was higher at 40 V (2743.35 J) than at 30 V (1852.97 J). This indicates that the amount of IONPs produced by the Joule heating effect increases as a function of the applied voltage up to 30 V, while no further increase occurs at 40 V. This suggests that the excess heat energy produced at 40 V was used to change the properties of IONPs by electrothermal annealing, rather than increasing their quantity. Figures 1(d–g) show photographs of the suspensions of IONPs electrosynthesized at different voltages before and after being exposed to a Nd magnet for up to 2 min. The samples synthesized at 10 V and 20 V demonstrated no response to the magnetic field while the samples synthesized at 30 V and 40 V appeared to be magnetic. The sample synthesized at 40 V visually shows the best magnetic response where dispersed NPs were completely separated from the solvent after just 2 min of exposure to the magnet. This indicates that the applied electrosynthesis voltage has a significant impact on the magnetic properties of the IONPs as discussed below.

IONPs were characterized using various techniques. Figure 2(a) shows the X-ray diffraction (XRD) patterns of IONPs synthesized at different voltages. The patterns demonstrate no distinct peaks for the samples synthesized at 10 V and 20 V, indicating their poor crystallinity or amorphous nature. On the other hand, the samples synthesized at 30 V and 40 V were crystalline, showing distinct peaks at 2θ values of 18.1, 30.2, 35.6, 43.3, 53.7, 57.3, and 62.9°. These peaks were indexed to the hkl planes (111), (220), (311), (400), (422), (511), and (440) in the γ - Fe_2O_3 (maghemite) phase^[35] agreeing with the JCPDS Card No. 00-039-1346. However, the sample synthesized at 40 V

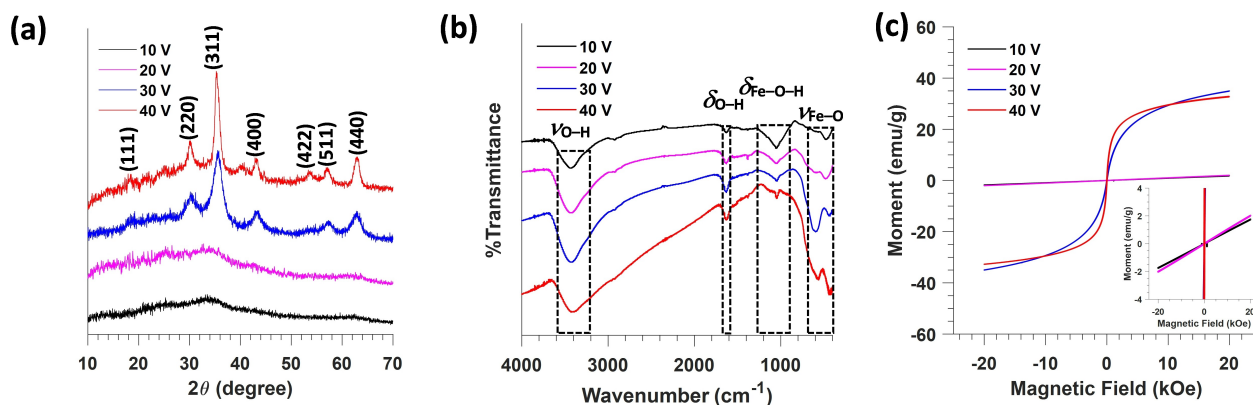
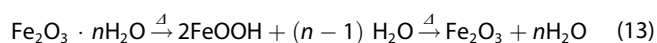


Figure 2. Characterization of IONPs synthesized at different voltages. (a) XRD patterns, (b) FTIR spectra, and (c) VSM magnetization curves.

shows an additional weak peak at $40.3^\circ 2\theta$ which can be attributed to the (113) plane in the $\alpha\text{-Fe}_2\text{O}_3$ (hematite) phase, according to the JCPDS Card No. 00-024-0072,^[4] with the other hematite peaks potentially overlapping with those of maghemite. This suggests that the higher voltage facilitates the synthesis of mixed phases of maghemite and hematite, but with hematite being present to a low extent. The improved crystallinity of the samples synthesized at 30 V and 40 V can be attributed to the high temperature generated during the electrosynthesis process at high voltages due to the Joule heating effect as discussed above. In other words, the material crystallinity was improved *via* electrothermal annealing. In addition, it can be noted that the IONPs synthesized at 40 V demonstrate narrower peaks indicating the highest crystallinity among all samples, which happened due to the high electrosynthesis temperature ($\sim 75^\circ\text{C}$). The crystallite size (D) was calculated for both crystalline samples synthesized at 30 V and 40 V using the (311) peak, being the most intense peak, and was found to be 4.8 nm and 8.3 nm, respectively. The increase in crystallite size with higher voltage suggests that the higher temperature and energy provided during the 40 V synthesis facilitated greater crystal growth, leading to larger crystallites.

Fourier Transform Infrared Spectroscopy (FTIR) spectra (Figure 2(b)) reveal characteristic bands in all samples. A band around 480 cm^{-1} , characteristic of Fe–O stretching ($\nu_{\text{Fe-O}}$) in FeOOH,^[36] was observed in all samples, along with another band in the range of $580\text{--}600\text{ cm}^{-1}$, attributed to Fe–O stretching in Fe_2O_3 .^[1] The FeOOH band was more pronounced in the samples synthesized at 10 V and 20 V, while the Fe_2O_3 band is more intense in the samples synthesized at 30 V and 40 V. Additionally, a band appeared in the range of $1050\text{--}1060\text{ cm}^{-1}$ in all samples, corresponding to the structural hydroxyl bending of Fe–O–H ($\delta_{\text{Fe-O-H}}$) in FeOOH.^[37] This band was most pronounced in the sample synthesized at 10 V and gradually diminishes as the synthesis voltage increases, indicating that the material consists primarily of FeOOH at low synthesis voltages, while Fe_2O_3 predominates at higher synthesis voltages. Furthermore, a minor band at 1630 cm^{-1} was present in all samples, which was attributed to hydroxyl bending ($\delta_{\text{O-H}}$) in adsorbed water.^[36] A broad, high-intensity band in the range of $3200\text{--}3600\text{ cm}^{-1}$, characteristic of the strongly absorbing O–H stretching vibrations, was also observed in all samples. This band becomes progressively broader as the synthesis voltage increases from 10 V to 30 V, with the sample synthesized at 40 V exhibiting the broadest band. The increased band broadness indicates the presence of significant hydrogen bonding interactions, particularly in the sample synthesized at 40 V, suggesting that H-bonding becomes more prominent at higher synthesis voltages. This can be ascribed to the protonation of surface hydroxyl groups.^[38] On this basis, we assume that $\text{Fe}_2\text{O}_3 \cdot n\text{H}_2\text{O}$, formed electrochemically (Eq. 5) and thermally (Eq. 12), converts into FeOOH upon mild heating (at 10 V and 20 V) and transforms into Fe_2O_3 at elevated temperature (at 30 V and 40 V) according to Eq. 13.



The magnetic properties of the synthesized IONPs were investigated using vibrating-sample magnetometry (VSM). Figure 2(c) shows the VSM curves, which indicate that the samples synthesized at 10 V and 20 V exhibit weak magnetic behavior with maximum magnetization (M_{max}) values of 1.8 emu/g and 2.0 emu/g, respectively. This is likely due to their poor crystallinity,^[39] and the significant presence of FeOOH, which is less magnetic than other iron oxides such as Fe_2O_3 or Fe_3O_4 .^[10] In contrast, the samples synthesized at 30 V and 40 V demonstrate higher M_{max} values of 34.0 emu/g and 32.9 emu/g, respectively, which can be attributed to their improved crystallinity.^[39] In addition, the absence of a hysteresis loop suggests a superparamagnetic behavior.^[17] However, the 40 V sample has slightly lower M_{max} than the 30 V sample likely due to the presence of hematite impurities in the former which is less magnetic than maghemite.^[11] Notably, the sample synthesized at 40 V saturates more readily than the one synthesized at 30 V, possibly due to the improved crystallinity of the former.^[40] This quicker attainment of saturation may account for the faster aggregation and separation of the NPs under the magnetic field, as shown in Figure 1(g).

Transmission electron microscopy (TEM) images in Figures 3(a) and 3(b) show that the samples synthesized at 10 V and 20 V do not consist of distinct nanoparticles but rather aggregates of ultrasmall, irregular particles that lack crystalline features. This suggests that the lower synthesis voltage results in poorly ordered or amorphous structures. The relatively low energy provided at 10 V and 20 V may not be sufficient to promote well-defined crystal growth. At a synthesis voltage of 30 V, the nanoparticles display a more uniform size and shape (Figure 3(c)) compared to those synthesized at 10 V and 20 V, with an average particle size of $6.5 \pm 1.0\text{ nm}$. The nanoparticles synthesized at 40 V exhibit a further improvement in uniformity (Figure 3(d)), with the particles being more spherical and well-defined, with a narrow size distribution of $9.6 \pm 1.2\text{ nm}$. However, some flake-like nanostructures co-exist with the nanospheres. The high-angle annular dark-field (HAADF) image (Figure 3(e)) shows that nanoflakes result in less electron scattering and thus appearing darker in the HAADF image. In contrast, the nanospheres appear brighter, indicating that they scatter more electrons, which suggests that they are denser than the nanoflakes. To better understand these structures, high-resolution (HR) TEM images were collected for both nanospheres (Figure 3(f)) and nanoflakes (Figure 3(g)). The corresponding d -spacings were estimated as 0.255 nm and 0.227 nm, respectively. The former corresponds to the (311) plane in maghemite ($\gamma\text{-Fe}_2\text{O}_3$),^[35] while the latter is attributed to the (113) plane in hematite ($\alpha\text{-Fe}_2\text{O}_3$).^[41] This indicates that the nanospheres are in the maghemite phase, representing the majority of the nanoparticles, whereas the nanoflakes are in the hematite phase which exists as a minor component. This is consistent with the XRD results discussed above. The formation of hematite nanoflakes in the 40 V sample could be due to the highly elevated temperature generated during synthesis. Although the HR-TEM image of a nanosphere (Figure 3(f)) shows that it is single crystalline, the SAED pattern obtained from a cluster of nanospheres (Figure 3(h)) displays concentric

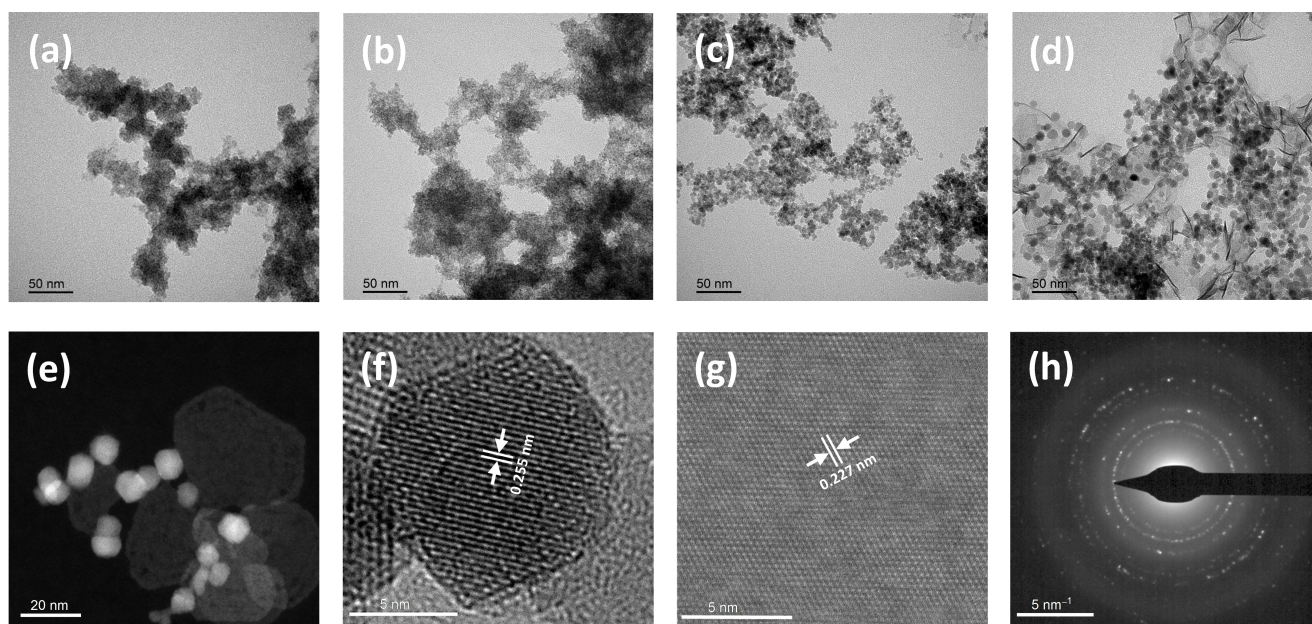


Figure 3. TEM images of IONPs synthesized at different voltages: (a) 10 V, (b) 20 V, (c) 30 V, and (d) 40 V. (e) HAADF image, (f) HR-TEM image of nanospheres, (g) HR-TEM image of nanoflakes, and (h) SAED pattern of nanospheres – all in the 40 V sample.

rings, suggesting that the nanospheres may exhibit multiple crystalline facets or are oriented differently within the cluster. As for nanoflakes, it was challenging to collect an SAED pattern for them as they are very thin. Overall, the higher synthesis voltage likely provides sufficient energy to promote better

crystal growth, resulting in more uniform and well-ordered IONPs.

Figure 4(a) shows the full-survey XPS spectra from which the elemental composition was identified and listed in Table 1. It can be observed that the Fe contents in the samples synthesized at 10 V and 40 V were $6.7 \pm 1.9\%$ and $25.0 \pm 0.2\%$,

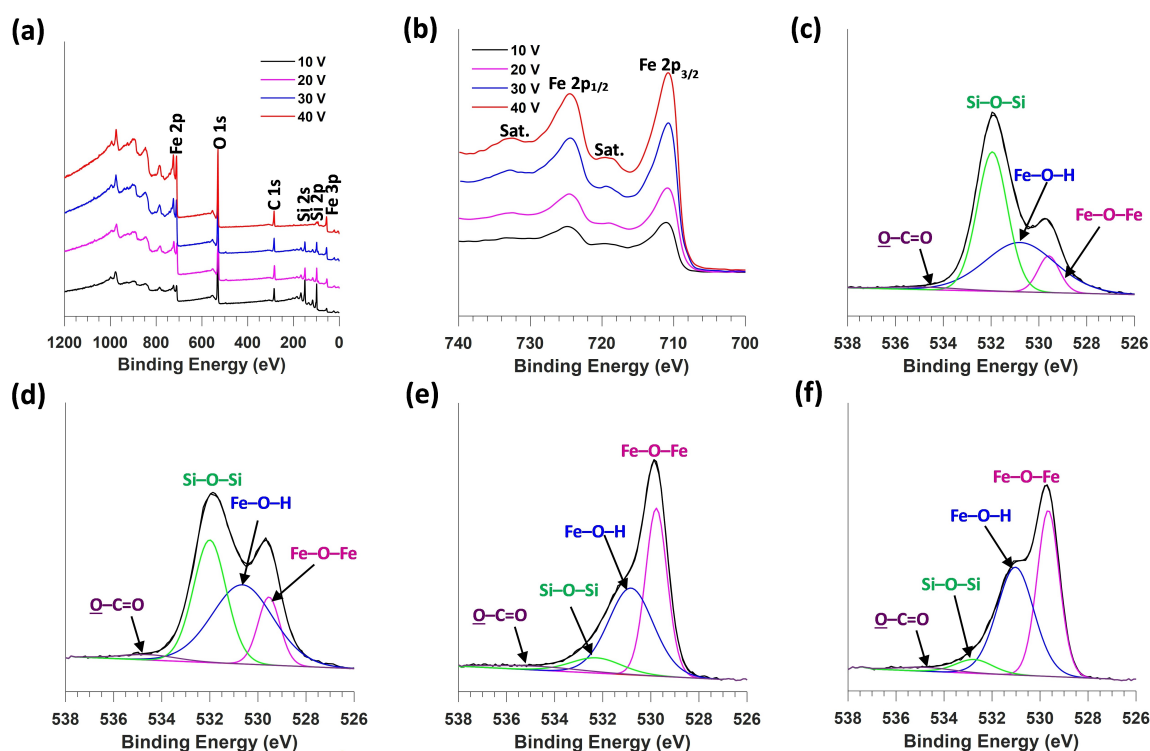


Figure 4. XPS analysis of IONPs synthesized at different voltages. (a) Full-survey spectra, (b) Fe 2p scans, and O 1s scans for the samples synthesized at (c) 10 V, (d) 20 V, (e) 30 V and (f) 40 V.

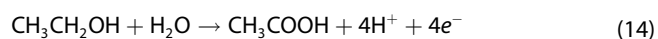
Table 1. Atomic composition obtained from XPS data for IONPs synthesized at different voltages (10–40 V). Values represent the mean \pm standard deviation ($n = 3$).

| Voltage (V) | Atomic composition (%) | | | |
|-------------|------------------------|----------------|----------------|----------------|
| | Fe | O | Si | C |
| 10 | 6.7 \pm 1.9 | 37.8 \pm 1.1 | 32.0 \pm 2.6 | 23.5 \pm 1.4 |
| 20 | 11.3 \pm 2.0 | 38.8 \pm 1.1 | 23.6 \pm 2.7 | 26.3 \pm 1.2 |
| 30 | 18.2 \pm 5.1 | 39.4 \pm 1.0 | 20.5 \pm 8.7 | 21.9 \pm 3.0 |
| 40 | 25.0 \pm 0.2 | 42.6 \pm 0.6 | 10.7 \pm 0.4 | 21.7 \pm 0.2 |

whereas the O contents were $37.8 \pm 1.1\%$ and $42.6 \pm 0.6\%$, respectively. The corresponding Fe:O ratios were 1:5.6 and 1:1.7, respectively, while the Fe:O ratio in Fe_2O_3 was theoretically 1:1.5. The excess O in all samples can be attributed to the native oxide film on the Si wafer substrate (on which IONPs were drop-cast), adsorbed water and/or hydroxyl groups on the surface of IONPs. Table 1 shows a decrease in Si content as the electrosynthesis voltage increases. This trend occurs because the same volume of IONP suspension (20 μL) was drop-cast on a Si wafer for each sample, whereas the obtained nanoparticle concentration in each suspension increased with the synthesis voltage, following the order: $10\text{ V} < 20\text{ V} < 30\text{ V} < 40\text{ V}$. The C content present was attributed to adventitious C and/or surface-adsorbed carbonaceous matter. The Fe 2p XPS scan is shown in Figure 4(b) which demonstrates two main peaks in all samples at $710.9 \pm 0.1\text{ eV}$ and another one at $724.6 \pm 0.1\text{ eV}$, corresponding to the Fe $2p_{3/2}$ and Fe $2p_{1/2}$ photoelectrons, respectively. In addition, there were two satellite peaks at approximately 718.9 ± 0.1 and $732.8 \pm 0.2\text{ eV}$, which are characteristic of the shake-up satellites often observed in the spectra of Fe^{3+} in iron oxides.^[14] The presence of Fe^{3+} species in the poorly crystalline samples synthesized at 10 V and 20 V suggests that both materials are primarily composed of Fe^{3+} -containing species. This corroborates the FTIR results showing that IONPs formed at 10 V and 20 V are likely in the form of FeOOH.

To further understand the different oxygen-based chemical environments in the electrosynthesized IONPs, O 1s XPS spectra were peak fitted into various oxygen components (Figures 4(c–f)). The corresponding binding energy and % area of each component are depicted in Table 2 for all samples. The O 1s spectra were fitted into three primary components: (a) lattice O in the iron oxide (Fe–O–Fe), (b) surface hydroxyl groups

(Fe–O–H), and (c) Si wafer native oxide layer (Si–O–Si). The calculated ratio of Fe–O–Fe to Fe–O–H components is 1:4.4 and 1:3.2 for the samples synthesized at 10 and 20 V, respectively. This suggests that both samples are mostly FeOOH rather than Fe_2O_3 . On the other hand, the ratio of those components is 1:1.1 in both samples synthesized at 30 V and 40 V. Given that both 30 V and 40 V samples were in the Fe_2O_3 form as inferred from XRD analysis, the equal ratio of lattice oxygen to hydroxyl oxygen suggests that the surface of those samples is covered by hydroxyl groups likely through the under-coordinated Fe atoms on the surface. In addition to those primary O components, there is a minor component (2.0–3.9%) that appeared at high binding energy range (534.5–534.9 eV) which can be attributed to O bound to a highly withdrawing group, likely carbonyl (C=O) in a carboxyl group (O–C=O).^[42–43] The peak fitting of the corresponding C 1s spectra (Figure S1) confirms the presence of carboxyl group (O–C=O) likely due to acetic acid (CH_3COOH). CH_3COOH may have formed by the partial electrooxidation of ethanol ($\text{CH}_3\text{CH}_2\text{OH}$), as shown in Eq. 14.^[44]



In conclusion, a synthesis voltage of 40 V is optimal for producing IONPs, as it results in fairly uniform nanoparticles with high crystallinity and enhanced magnetic properties. In addition, the highest yield of nanoparticles was achieved at this voltage, which can be further increased by extending the electrosynthesis time. This is because as the amount of IONPs produced is directly proportional to the electric charge passed, which increases with time (Eq. 6). Therefore, IONPs synthesized at 40 V were selected for the subsequent surface modification step using various silane reagents, including TEOS, MPTMS, and APTES, which was also conducted electrochemically.

2.2. Nanoparticle Silanization and Characterization

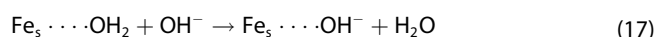
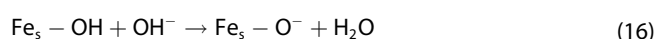
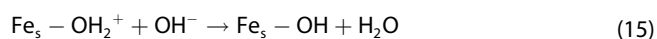
IONPs were modified with TEOS, MPTMS, and APTES using an electrochemical setup consisting of a Pt anode and a graphite cathode. The Pt cathode was employed to generate OH^- ions through water electrolysis (as shown in Eq. 2), while the graphite anode was chosen for its low electrocatalytic activity towards the electrooxidation of both ethanol^[45] and water.^[46] As a result, the anodic (oxidation) reaction at the graphite anode is proposed to primarily involve the electrosorption of negatively

Table 2. Binding energy positions and % area for fitted O 1s scans in IONPs synthesized at different voltages (10–40 V).

| Voltage (V) | Fe–O–Fe | | Fe–O–H | | Si–O–Si | | O–C=O | |
|-------------|---------------|----------|---------------|----------|---------------|----------|---------------|----------|
| | Position (eV) | Area (%) | Position (eV) | Area (%) | Position (eV) | Area (%) | Position (eV) | Area (%) |
| 10 | 529.68 | 9.15 | 530.87 | 40.16 | 532.03 | 48.68 | 534.78 | 2.01 |
| 20 | 529.53 | 14.09 | 530.64 | 45.37 | 531.99 | 37.78 | 534.53 | 2.76 |
| 30 | 529.89 | 42.14 | 530.95 | 44.98 | 532.39 | 8.98 | 534.89 | 3.90 |
| 40 | 529.66 | 44.05 | 531.03 | 47.43 | 532.75 | 6.07 | 534.76 | 2.45 |

charged OH^- ions onto the positively charged graphite electrode surface, rather than the oxidation of ethanol or water. Therefore, this setup ensures the continuous generation of OH^- ions, which can catalyze the hydrolysis and condensation of organosilanes in a manner similar to the Stöber method but with more control over the amount of OH^- ions provided to the system. We propose that in our protocol, the organosilanes undergo electrochemical hydrolysis and condensation through a process we term “Electro-alkaline Titration” (EAT). This term refers to the controlled *in-situ* generation and utilization of OH^- ions to facilitate the silanization process, ensuring precise control over the reaction conditions and leading to the formation of well-defined silane-modified Fe_2O_3 with optimized properties.

To investigate this postulation, IONPs were electrochemically treated in an electrolyte consisting of 50 mM LiCl in ethanol (with 5% H_2O), and the resulting surface changes were investigated using zeta potential measurements. The pristine (unmodified) Fe_2O_3 NPs have a zeta potential of $+27.6 \pm 0.5$ mV which suggests that the surface hydroxyl groups on the Fe_2O_3 NPs are protonated,^[47–48] likely by the protons generated due to the ethanol electrooxidation (Eq. 14). This is also reflected in the broadening of the hydroxyl-related FTIR stretching band ($3600\text{--}3200\text{ cm}^{-1}$) (Figure 2(b)). Upon electrochemical treatment, the measured zeta potential changed to -25.2 ± 1.6 mV suggesting that the surface hydroxyl groups on the Fe_2O_3 surface were restored. This indicates that the Fe_2O_3 surface was activated and enriched with hydroxyl groups, i.e., hydroxylated. Two modes are suggested for surface activation by hydroxylation; (i) deprotonation of protonated surface hydroxyl groups attached to surface Fe atoms (Fe_s) by the generated OH^- ions (Eq. 15), possibly along with a subsequent deprotonation of the restored or pre-existing hydroxyl groups (Eq. 16) and (ii) the replacement of water molecules, pre-adsorbed on the oxide surface *via* Fe atoms, with hydroxyl groups (Eq. 17).



The surface chemistry of the hydroxylated Fe_2O_3 was further studied using XPS analysis. Figure S2(a) compares the Fe 2p scans in both pristine and hydroxylated Fe_2O_3 samples which show no change in peak positions indicating no change in the Fe oxidation state, and thus no change in the oxide bulk. This also suggests that surface Fe atoms were not involved in the hydroxylation step. In other words, surface hydroxylation by replacing water molecules with hydroxide ions (Eq. 17) is unlikely to have happened. Surface O-based species were quantified by fitting the O 1s scan in Figure S2(b). Table S2 shows that the % area of Fe–O–H increased from 47.43% to 59.83% after hydroxylation indicating the successful surface hydroxylation, most likely *via* restoring hydroxyl groups following Eq. 15.

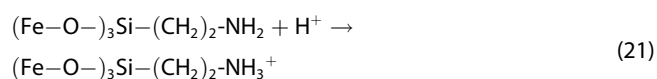
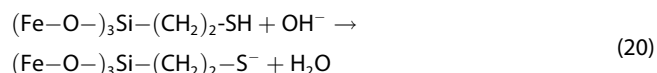
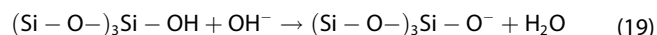
Surface modification of oxides with organosilanes typically occurs through two main steps: (i) the hydrolysis of organosilane molecules and (ii) the condensation of these hydrolyzed molecules with hydroxyl groups on the oxide surface.^[49] The medium pH has a significant influence on the hydrolysis and condensation of organosilanes. The hydrolysis is promoted at low pH facilitating the formation of silanol (Si-OH) groups,^[50–51] while the condensation happens with a slow rate.^[19, 52] Both hydrolysis and condensation are slow at neutral pH.^[19] At high pH, the hydrolysis still occurs but with a slower rate than at low pH,^[53] whereas the condensation is significantly promoted.^[51, 54] In our electrochemical system, the Fe_2O_3 /silane coupling experiments were conducted electrochemically in a non-aqueous (ethanol-based) electrolyte, which made it challenging to directly measure the medium pH. However, based on the understanding of our electrochemical system and the associated fundamental electrochemical reactions, it is clear that the medium is rich in OH^- ions generated due to water electrolysis, as confirmed by the hydroxylation of the IONPs. Therefore, it can be postulated that in this alkaline environment, silane molecules are more likely to undergo direct condensation with Fe_2O_3 surface hydroxyl groups. The silane condensation can also occur between silane molecules themselves (self-condensation), and this is promoted at high temperatures.^[55] So, the silanization was conducted under vigorous stirring to reduce the heat generated due to the Joule heating effect (Figure S3). To ensure that only Fe_2O_3 -bound silanes remained, the silane-modified IONPs were separated from the reaction medium and thoroughly washed *via* magnetic decantation to remove self-condensed silanes. Thus, in this electrochemical silanization protocol – we refer to this as “Electrosilanization” – Fe_2O_3 NPs were directly grafted with organosilanes by simply adding the silane reagent to the electrolyte. The NPs were *in-situ* enriched with hydroxyl groups, and reacted directly with the silane *via* alcohol condensation, eliminating the need for both pre-activation of the NP surface and pre-hydrolysis of the silanes.

The silane modification of IONPs using TEOS, MPTMS, and APTES was investigated through zeta potential measurements at pH 7. As shown in Table 3, the zeta potential of pristine IONPs changed from $+27.6 \pm 0.5$ mV to -41.3 ± 1.5 mV after modification with TEOS, suggesting the successful coating of Fe_2O_3 with a SiO_2 layer. The significant negative charge observed after coating with SiO_2 is due to the deprotonation of silanol groups (Si-OH), which occurs when they react with OH^- ions, formed by the dissociation of water (Eq. 18), as shown in Eq. 19. This is because the point of zero charge (PZC) – the pH

Table 3. Zeta potentials measured for Fe_2O_3 nanoparticles (IONPs) before and after modification with TEOS, MPTMS, and APTES. Values represent the mean \pm standard deviation ($n = 3$).

| Sample | Zeta Potential (mV) |
|--------------------------------------|---------------------|
| Fe_2O_3 | $+27.6 \pm 0.5$ |
| $\text{Fe}_2\text{O}_3/\text{TEOS}$ | -41.3 ± 1.5 |
| $\text{Fe}_2\text{O}_3/\text{MPTMS}$ | -18.8 ± 0.5 |
| $\text{Fe}_2\text{O}_3/\text{APTES}$ | $+16.2 \pm 0.2$ |

at which the net surface charge is zero^[48] – is typically around pH 2.8 for SiO₂^[56] compared to pH 8.0 for γ -Fe₂O₃.^[57] For the Fe₂O₃ modified with MPTMS and APTES, the measured zeta potentials were -18.8 ± 0.5 mV and $+16.2 \pm 0.2$ mV, respectively, indicating successful functionalization of the Fe₂O₃ surface with thiol (–SH) and amine (–NH₂) groups, respectively. The negative surface charge observed after thiol functionalization is due to the deprotonation of the thiol group (Eq. 20), whereas the positive surface charge after amine functionalization results from the protonation of the amine group (Eq. 21) in the aqueous medium. 820



The FTIR spectra collected for all modified IONPs (Figure 5(a)) show the characteristic Fe–O stretching bands which are attributed to the Fe₂O₃ as discussed above. This indicates that no change happened to the Fe₂O₃ bulk. Upon modification with the different organosilanes, a broad band emerged between 970 cm^{−1} and 1190 cm^{−1}, showing overlapping peaks at: (i) 1050 cm^{−1} that correspond to asymmetric Si–O–Si stretching, indicative of the siloxane (Si–O–Si) network,^[58–59]

and (ii) 1130 cm^{−1} relating to asymmetric Si–O–C stretching,^[60–61] indicating incomplete silane hydrolysis. Si–O–C bands were particularly observed in the Fe₂O₃/TEOS and Fe₂O₃/APTES samples, in which incomplete hydrolysis was further confirmed by a band at 1490 cm^{−1}, attributed to C–H bending in the CH₃ groups of Si–O–CH₂CH₃.^[60] In addition, there was a broad band around 3400 cm^{−1} in all samples as a result of O–H stretching.^[59] Both Fe₂O₃/MPTMS and Fe₂O₃/APTES spectra showed weak peaks around 1440 cm^{−1} and 2920 cm^{−1} due to C–H bending and stretching, respectively, in the methylene (CH₂) segments^[18, 62] in $-(\text{CH}_2)_3-\text{SH}$ and $-(\text{CH}_2)_3-\text{NH}_2$, respectively. The absence of the characteristic band of SH, which usually appears as a weak peak at around 2550 cm^{−1},^[49, 62] suggests a very low concentration of SH groups on the NP surface, or their partial or complete transformation to other S-based species as will be discussed later. The N–H stretching peak in Fe₂O₃/APTES could have overlapped with that of O–H stretching, and thus appeared together around 3400 cm^{−1}.^[63]

The full XPS survey spectra (Figure 5(b)) confirmed the presence of Si in all modified Fe₂O₃ samples, with particularly high levels in the TEOS-modified sample. Table 4 provides the XPS-based elemental composition of all samples, obtained by quantifying XPS spectra. The % area of Si was $12.0 \pm 0.6\%$ in the Fe₂O₃/MPTMS sample, which was low compared to the Fe₂O₃/TEOS ($21.0 \pm 2.3\%$) and Fe₂O₃/APTES ($17.7 \pm 1.2\%$) samples. Conversely, the % area of Fe was $20.0 \pm 0.3\%$ in the Fe₂O₃/MPTMS sample, compared to $3.6 \pm 0.4\%$ in the Fe₂O₃/TEOS and $9.2 \pm 0.6\%$ in the Fe₂O₃/APTES samples. This suggests that Si-based layers have formed on the Fe₂O₃ surface in all cases, but with the layer being thinner in Fe₂O₃/MPTMS compared to

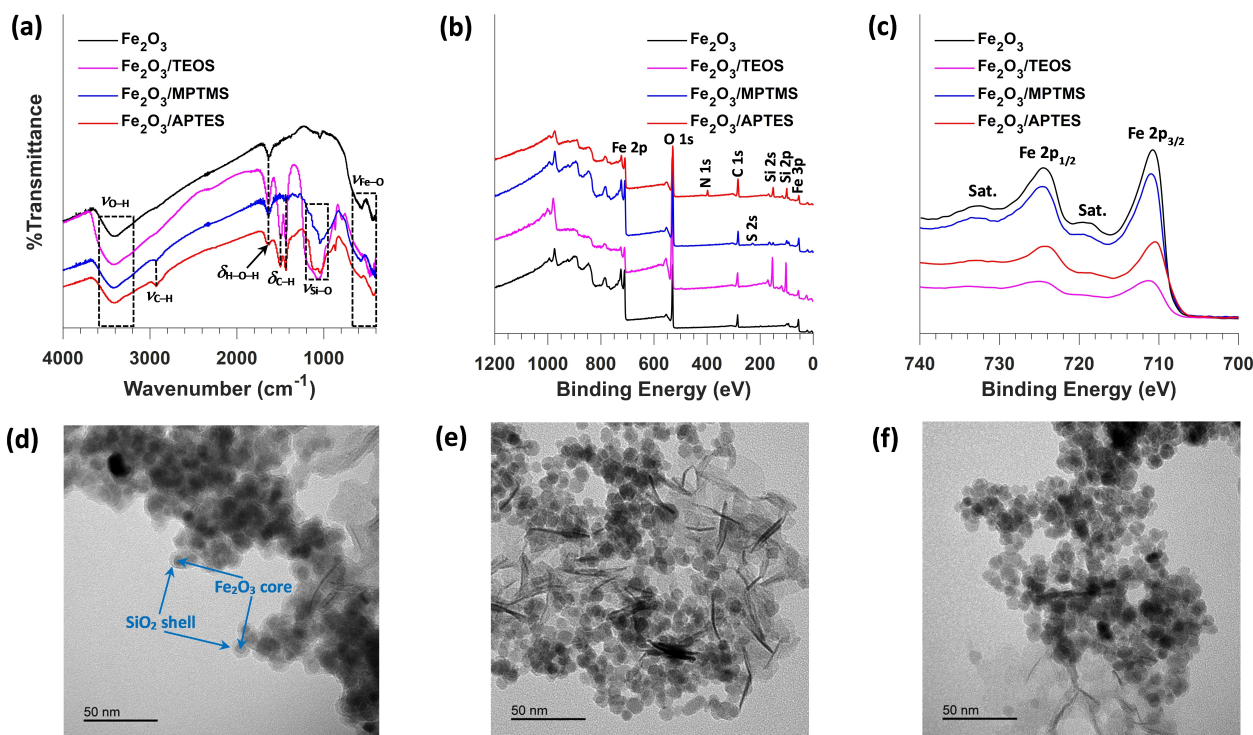
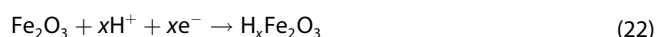


Figure 5. Characterization of Fe₂O₃ nanoparticles (IONPs) modified with TEOS, MPTMS, and APTES. (a) FTIR spectra, (b) XPS full survey, (c) HR Fe 2p scans, and TEM images of (d) TEOS-modified, (e) MPTMS-modified, and (f) APTES-modified IONPs.

Table 4. Atomic composition obtained from XPS data for Fe₂O₃ nanoparticles (IONPs) before and after modification with TEOS, MPTMS, and APTES. Values represent the mean \pm standard deviation ($n=3$).

| Sample | Atomic composition (%) | | | | | |
|---------------------------------------|------------------------|----------------|----------------|----------------|---------------|---------------|
| | Fe | O | Si | C | S | N |
| Fe ₂ O ₃ | 25.0 \pm 0.2 | 42.6 \pm 0.6 | 10.7 \pm 0.4 | 21.7 \pm 0.2 | N/A | N/A |
| Fe ₂ O ₃ /TEOS | 3.6 \pm 0.4 | 58.7 \pm 3.4 | 21.0 \pm 2.3 | 16.7 \pm 0.6 | N/A | N/A |
| Fe ₂ O ₃ /MPTMS | 20.0 \pm 0.3 | 44.2 \pm 0.5 | 12.0 \pm 0.6 | 21.5 \pm 0.3 | 2.4 \pm 0.0 | N/A |
| Fe ₂ O ₃ /APTES | 9.2 \pm 0.6 | 37.5 \pm 1.2 | 17.7 \pm 1.2 | 31.0 \pm 0.9 | N/A | 4.6 \pm 0.2 |

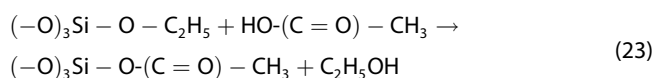
Fe₂O₃/APTES, and thickest in the Fe₂O₃/TEOS sample. The thinner silane layer in the Fe₂O₃/MPTMS sample compared to the Fe₂O₃/APTES sample was further confirmed by the corresponding % area of S (2.4 \pm 0.0%) and N (4.6 \pm 0.2%). The Fe 2p scan in Figure 5(c) showed that there was almost no change in the shape and position of the characteristic Fe³⁺ peaks across both the Fe₂O₃/TEOS and Fe₂O₃/MPTMS samples compared to the pristine Fe₂O₃. In the APTES-modified Fe₂O₃ sample, the Fe 2p peaks exhibited a slight shift towards lower binding energies, suggesting that Fe³⁺ species was partially reduced, possibly by electrochemical proton intercalation (Eq. 22). It appears that APTES molecules act as proton carriers *via* their amino groups, which readily protonate and subsequently transfer protons from the solution bulk to the surface of Fe₂O₃ nanoparticles during Fe₂O₃-APTES interactions. In addition, the relative intensity of the Fe 2p signal is higher in the MPTMS-modified Fe₂O₃ compared to the TEOS- and APTES-modified samples, further suggesting that a thinner layer has formed on the Fe₂O₃ surface in the MPTMS-modified Fe₂O₃. In contrast, the TEOS-modified Fe₂O₃ shows the least Fe 2p relative intensity, indicating the formation of a thick SiO₂ coating. TEM images (Figures 5(d-f)) corroborate these findings, showing a thick SiO₂ coating on the Fe₂O₃ surface in the TEOS-modified sample forming Fe₂O₃@SiO₂ core-shell structure. On the other hand, the Fe₂O₃ modifications with MPTMS and APTES did not result in thick coatings.



To better understand the chemical environments on the modified Fe₂O₃ surface, high-resolution XPS scans of various surface elements were peak fitted. Figure 6(a) presents the peak fitted Si 2p scan for the Fe₂O₃/TEOS, Fe₂O₃/MPTMS, and Fe₂O₃/APTES samples. Peaks corresponding to Si–O–Fe were observed in all samples at binding energies of 101.5–101.9 eV, while the broad peaks at 103.2–103.4 eV can be attributed to siloxane (Si–O–Si) networks.^[8] It should be noted that the peaks due to silanol (Si–OH) bonds significantly overlap with those of siloxane (Si–O–Si) bonds, making it difficult to separate these components using spectra collected from conventional XPS.^[64] The % area of the Si–O–Fe component follows the order Fe₂O₃/TEOS (12.4%) < Fe₂O₃/APTES (31.6%) < Fe₂O₃/MPTMS (78.8%), with the reverse trend observed for the Si–O–Si component. This suggests that MPTMS forms more silane linkages with the Fe₂O₃ surface (Si–O–Fe) compared to APTES, which in turn

forms more Si–O–Fe bonds than TEOS. The Fe₂O₃/MPTMS and Fe₂O₃/APTES samples exhibited peaks in the low binding energy range of 99.5–100.1 eV, which are attributed to Si–C bonds.^[61] Moreover, the Fe₂O₃/TEOS and Fe₂O₃/APTES samples showed specific peaks at 102.5–102.7 eV, attributed to Si–O–C bonds^[63] from residual ethoxysilane groups of non-hydrolyzed species, corroborating FTIR results. This is unlike MPTMS which appeared to have undergone complete hydrolysis, where the methoxy group generally hydrolyzes more readily than the ethoxy group.^[19] The Fe₂O₃/TEOS sample exhibited an unexpected peak at 105.9 eV, which may be attributed to Si in proximity to a highly electron-withdrawing group, suggested to be a carbonyl group (C=O) of a carboxylic acid.

Figure 6(b) showed two corresponding O 1s peaks at binding energies of 530.8 and 535.0 eV, obtained with their % area fixed at a 1:1 ratio,^[42] which can be assigned to O–C=O and O–C–O, respectively.^[42–43] This assignment was confirmed by the O–C–O component at a binding energy of 288.3 eV in the peak fitted C 1s scan (Figure S4(a)). The presence of this component in the Fe₂O₃/TEOS sample in significant amounts suggests that the ethoxy group in the ethoxysilane on the SiO₂ surface has undergone esterification, possibly by acetic acid formed during ethanol electrooxidation (Eq. 23).



All samples showed O 1s peaks at binding energies of 529.6–529.7 eV, 530.7–530.9 eV and 531.8–532.3 eV, which can be attributed to Fe–O–Fe, Si–O–Fe and Si–O–Si bonds, respectively.^[65–66] However, the Fe₂O₃/APTES sample revealed another component at 528.0 eV (Fe'–O–Fe'), suggesting the presence of Fe in a slightly reduced oxidation state (less than +3), corroborating the observed shift in Fe 2p peaks (Figure 5(c)). This indicates that APTES molecules facilitate the proton transfer to Fe₂O₃ surface leading to proton intercalation into Fe₂O₃, as discussed earlier (Eq. 22). From the O 1s spectra (Figure 6(b)), it can be observed that the Si–O–Fe peaks exhibited a higher % area in Fe₂O₃/MPTMS compared to Fe₂O₃/APTES and Fe₂O₃/TEOS, while the latter showed the highest % area for the Si–O–Si peak. These findings align with the observations from the Si 2p scans mentioned above, suggesting that MPTMS preferentially forms monolayers on the Fe₂O₃ surface through its three silane groups, whereas APTES tends to form oligomers. In contrast, TEOS molecules polymerize on the

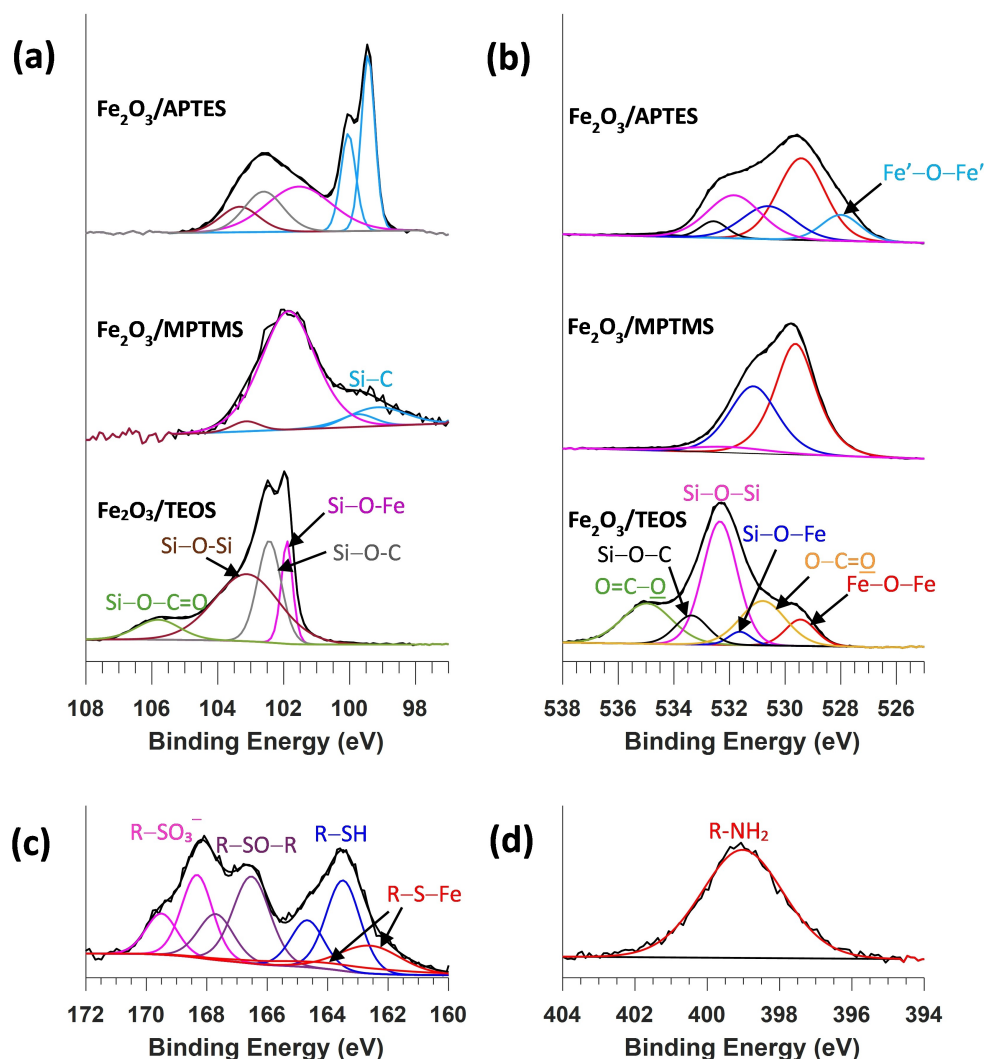


Figure 6. Fitting HR-XPS scans in silane-modified IONPs. (a) Si 2p and (b) O 1s scans in Fe₂O₃/TEOS, Fe₂O₃/MPTMS, and Fe₂O₃/APTES. (c) S 2p scan in Fe₂O₃/MPTMS. (d) N 1s scan in Fe₂O₃/APTES.

Fe₂O₃ surface *via* crosslinking within the Si–O–Si network, resulting in a thick SiO₂ coating, as evidenced by the TEM images. Both Fe₂O₃/TEOS and Fe₂O₃/APTES samples showed O 1s peaks at 532.6–533.4 eV, which can be attributed to Si–OH bonds,^[64] and/or Si–O–C bonds,^[67] possibly from non-hydrolyzed ethoxysilanes.

For the Fe₂O₃/MPTMS sample, Figure 6(c) shows the peak fitted S 2p scan, which includes multiple components. A doublet was considered for each component with an energy separation of 1.2 eV, to account for the spin-orbit splitting between S 2p_{1/2} and S 2p_{3/2}^[49] and the area ratio was constrained to 1:2.^[42] Four components appeared at S 2p_{1/2}/S 2p_{3/2} binding energies of 163.6/162.4, 164.7/163.5, 167.7/166.5, and 169.5/168.3 eV, corresponding to thiolates^[68–69] (R–S–Fe), thiol groups (R–SH),^[49, 70] sulfoxide (R–SO–R), and sulfonate groups (R–SO₃[−]),^[70] respectively. The presence of sulfur in oxidized states indicates the oxidation of the thiol group.^[71] The relevant S–O peaks appeared to have overlapped with the Si–O peaks. This partial oxidation of thiols could have occurred either

through electrooxidation at the anode or due to the heat generated during the electrosilanization process. Figure S3(a) shows that more current was recorded during the electrosilanization of Fe₂O₃ with MPTMS than with TEOS and APTES, indicating that some of the electric charge was used for thiol oxidation. As for the Fe₂O₃/APTES sample, the N 1s scan (Figure 6(d)) showed a single component at 399.0 eV attributed to the amine group (NH₂).^[68]

The scheme depicted in Figure 7 provides a summary of the electrosilanization process. Initially, water molecules electrolyze to produce OH[−] ions, which play a dual role: facilitating the hydrolysis of silane molecules and activating the Fe₂O₃ surface by restoring hydroxyl groups. TEOS, MPTMS, and APTES undergo hydrolysis at different rates, catalyzed by both OH[−] ions and the heat generated due to the Joule heating effect. Among these silanes, MPTMS likely hydrolyzes the fastest because its methoxy groups (Si–O–CH₃) hydrolyze more rapidly than the ethoxy groups (Si–O–C₂H₅) in TEOS and APTES. Once fully or partially hydrolyzed, the silane molecules condense, through

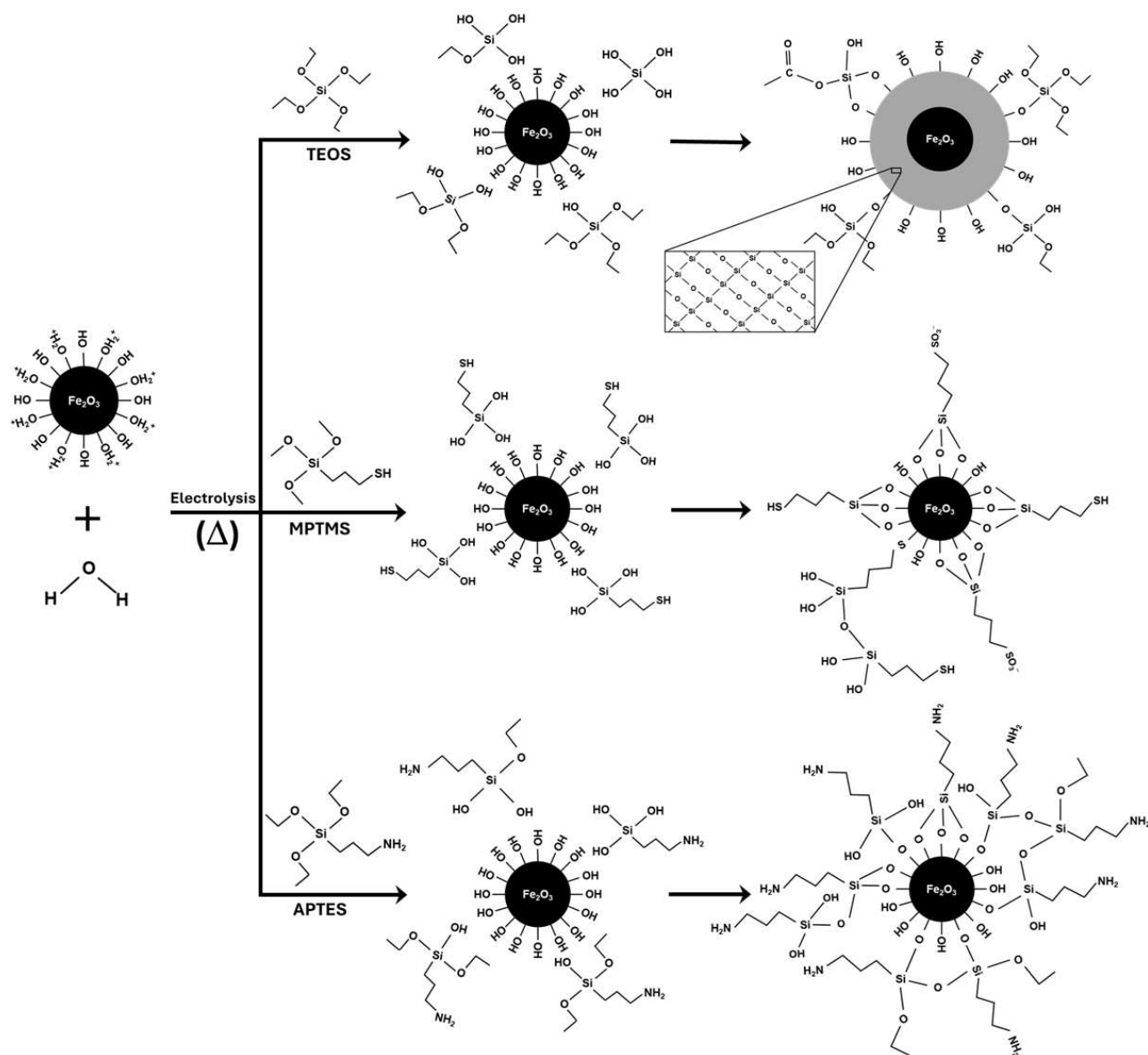


Figure 7. Schematic of the electrosilanization process for Fe_2O_3 nanoparticles with TEOS, MPTMS and APTES.

their silanol groups ($\text{Si}-\text{OH}$), with hydroxyl groups on the Fe_2O_3 surface, resulting in the removal of water (H_2O) molecules as a condensation by-product. TEOS- and APTES-modified Fe_2O_3 nanoparticles further interact with other TEOS and APTES molecules which are mostly partially hydrolyzed. Meanwhile, the SH groups on MPTMS-modified Fe_2O_3 undergo oxidation forming other species such as sulfonate and sulfoxide groups. Moreover, a portion of the MPTMS molecules form $\text{R}-\text{S}-\text{Fe}$ bonds by condensing their thiol groups with hydroxyl groups on the Fe_2O_3 surface. TEOS molecules, in particular, undergo significant polymerization resulting in a thick SiO_2 coating forming $\text{Fe}_2\text{O}_3@\text{SiO}_2$ core-shell structure. In contrast, MPTMS tends to form a monolayer, while APTES likely favors oligomer formation on the Fe_2O_3 surface via $\text{Si}-\text{O}-\text{Si}$ linkages. This sequence of Fe_2O_3 surface activation, silane hydrolysis, and Fe_2O_3 -silane coupling through condensation highlights the

complex chemistry involved in electrosilanization, yielding varied surface modifications depending on the silane used.

2.3. Magnetic Removal of Lead Ions

2.3.1. Effect of Surface Modification

The potential application of silane-modified IONPs for the magnetic removal of Pb^{2+} ions was investigated under neutral pH conditions. TEOS-, MPTMS-, and APTES-modified IONPs were tested in 50 ppm solutions of Pb^{2+} ions at pH 7. The equilibrium concentrations (C_e , ppm) of Pb^{2+} ions were determined using inductively coupled plasma optical emission spectroscopy (ICP-OES), and these values were used to calculate the adsorption capacity (q_{eq} , mg/g) for each sample according to Eq. 24.^{[1], [4]}

$$q_e = \frac{C_0 - C_e}{m} V \quad (24)$$

where C_0 is the initial Pb^{2+} ion concentration (ppm "mg/L"), C_e is the equilibrium concentration of Pb^{2+} ions remaining after treatment with the nanoparticles, V is the volume of the Pb^{2+} ion solution (L), and m is the mass of the nanoparticles (g). It is important to note that C_0 was also determined for the as-prepared solutions using ICP-OES measurements as Pb^{2+} ions tend to precipitate from solutions in the form of $\text{Pb}(\text{OH})_2$, particularly at neutral and alkaline pH levels.^[72] This approach ensures an accurate calculation of C_0 and q_e . In addition, to ensure the repeatability of the measurements, two sets of pristine and modified nanoparticles were independently synthesized and tested for the Pb^{2+} ion removal. The corresponding removal efficiency (%R) was calculated from Eq. 25.^[3, 7]

$$\%R = \frac{(C_0 - C_e)}{C_0} \times 100 \quad (25)$$

Figure 8(a) shows that the adsorption capacity (q_e) values calculated for pristine, TEOS-, MPTMS-, and APTES-modified IONPs were 42.9 ± 6.5 , 79.4 ± 12.9 , 38.1 ± 0.9 , and 80.1 ± 12.9 mg/g, respectively. Notably, the q_e value for MPTMS-modified IONPs was unexpectedly lower compared to that of

the unmodified IONPs. In contrast, the TEOS- and APTES-modified IONPs exhibited nearly double the adsorption capacity of unmodified IONPs. Both TEOS- and APTES-modified IONPs exhibit exceptionally high removal efficiencies, at $98.0 \pm 0.4\%$ and $98.8 \pm 0.2\%$, respectively. In contrast, MPTMS-modified IONPs demonstrate the lowest removal efficiency ($47.5 \pm 6.4\%$), which is even lower than that of the unmodified IONPs ($53.0 \pm 0.4\%$), reflecting a similar trend to the q_e values.

The mechanism of Pb^{2+} ion adsorption was investigated using *ex-situ* (post-treatment) XPS analysis to compare the surface chemical environments of nanoparticles after treatment in Pb^{2+} ion solutions with their fresh states. Figure 8(b) presents the full-survey XPS spectra, which showed that Pb element remained in all samples collected from Pb^{2+} ion solutions, even after washing with water. This indicated that Pb^{2+} ions strongly bind to the nanoparticle surfaces through surface functional groups. Table 5 summarizes the corresponding atomic composition obtained from XPS data for all nanoparticles. The $\text{Fe}_2\text{O}_3/\text{TEOS}$ sample exhibited the highest Pb^{2+} ion content ($1.7 \pm 0.1\%$), which can be attributed to the high porosity of the SiO_2 shell and the presence of surface functional groups, resulting in a high adsorption capacity for Pb^{2+} ions. $\text{Fe}_2\text{O}_3/\text{APTES}$ follows $\text{Fe}_2\text{O}_3/\text{TEOS}$ with a Pb elemental content of $1.3 \pm 0.0\%$, while the pristine and MPTMS-modified Fe_2O_3 show the lowest Pb elemental content ($0.6 \pm 0.0\%$). To further explore the Pb^{2+}/NP binding mechanism, high resolution XPS scans were collected

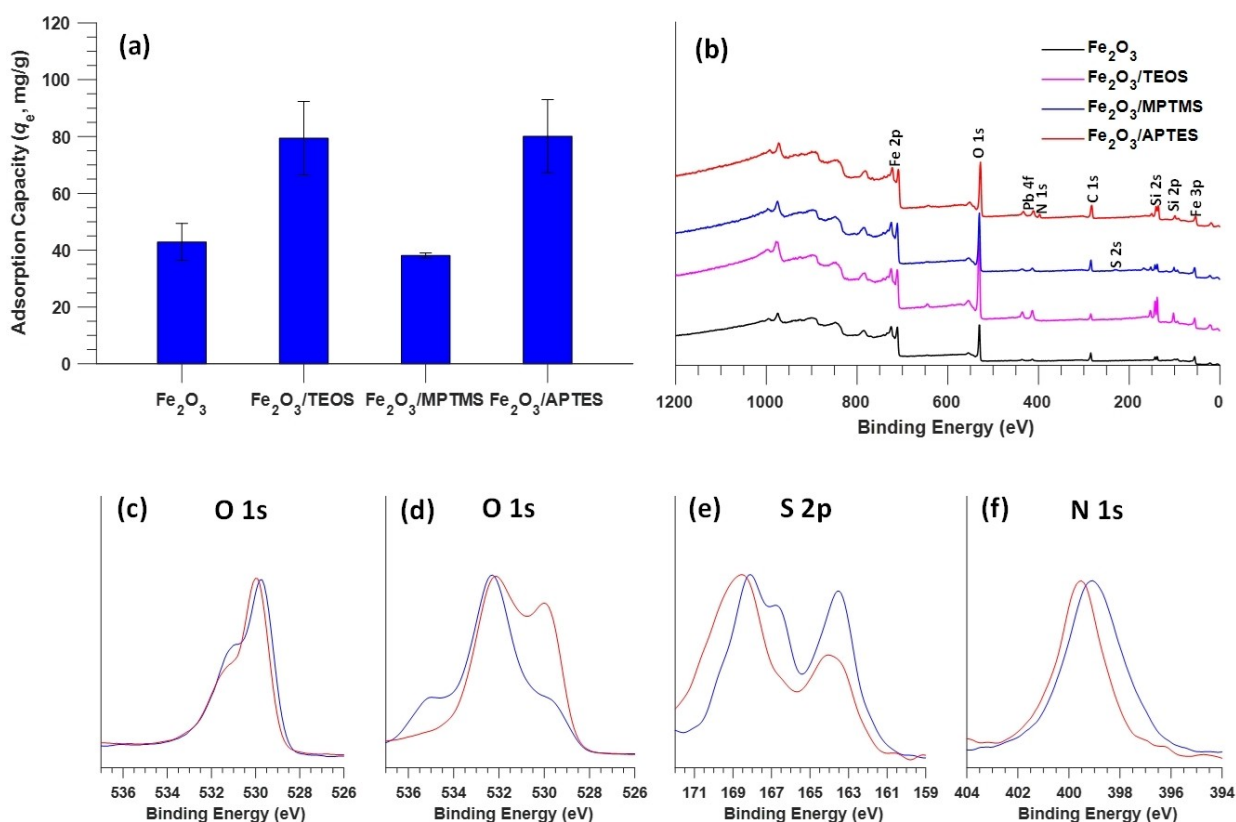


Figure 8. (a) Adsorption capacity of pristine and silane-modified IONPs for Pb^{2+} ion removal from aqueous solutions. Values presented are mean (%) for two independent samples of each material \pm standard deviation ($n=2$). (b) XPS Full surveys of pristine and silane-modified Fe_2O_3 nanoparticles after Pb^{2+} -ion adsorption. (c) O 1s scan in Fe_2O_3 , (d) O 1s scan in $\text{Fe}_2\text{O}_3/\text{TEOS}$, (e) S 2p scan in $\text{Fe}_2\text{O}_3/\text{MPTMS}$, and (f) N 1s scan in $\text{Fe}_2\text{O}_3/\text{APTES}$ before (blue curve) and after (red curve) Pb^{2+} -ion adsorption.

Table 5. Atomic composition obtained from XPS data for pristine and silane-modified IONPs after Pb²⁺-ion adsorption. Values represent the mean \pm standard deviation ($n=3$).

| Sample | Atomic composition (%) | | | | | | |
|---------------------------------------|------------------------|----------------|----------------|----------------|---------------|---------------|---------------|
| | Fe | O | Si | C | S | N | Pb |
| Fe ₂ O ₃ | 23.8 \pm 0.8 | 41.0 \pm 0.5 | 10.0 \pm 1.4 | 24.5 \pm 0.6 | N/A | N/A | 0.6 \pm 0.0 |
| Fe ₂ O ₃ /TEOS | 14.9 \pm 0.4 | 56.4 \pm 2.2 | 15.3 \pm 3.9 | 11.7 \pm 2.3 | N/A | N/A | 1.7 \pm 0.1 |
| Fe ₂ O ₃ /MPTMS | 18.8 \pm 1.0 | 43.8 \pm 1.3 | 12.2 \pm 0.6 | 22.1 \pm 2.2 | 2.4 \pm 0.5 | N/A | 0.6 \pm 0.0 |
| Fe ₂ O ₃ /APTES | 15.7 \pm 0.6 | 40.6 \pm 0.3 | 11.4 \pm 0.5 | 27.8 \pm 0.3 | N/A | 3.2 \pm 0.2 | 1.3 \pm 0.0 |

for O 1s in both Fe₂O₃ and Fe₂O₃/TEOS, S 2p in Fe₂O₃/MPTMS and N 1s in Fe₂O₃/APTES. In Figure 8(c), the O 1s peak of the pristine Fe₂O₃ at 529.7 eV, attributed to the Fe–O–Fe bond, shifts to 530 eV after Pb²⁺ ion adsorption, suggesting that Pb²⁺ ions coordinate with surface oxygen atoms, possibly via their lone pairs. Moreover, the intensity of the peak at 530.0 eV, corresponding to surface hydroxyl groups (Fe–O–H), slightly decreased, indicating that these groups may have been partially broken to form bonds with Pb²⁺ ions, resulting in the formation of Fe–O–Pb. Given the highly positive zeta potential of this material, likely due to hydroxyl group protonation, another plausible mechanism for Pb²⁺ ion adsorption could be the ion exchange between protons (H⁺) and Pb²⁺ ions. For Fe₂O₃/TEOS (Figure 8(d)), a significant peak at around 530.0 eV has emerged which suggests the formation of Si–O–Pb^[73] via covalent binding between Pb²⁺ ions and hydroxyl groups on the SiO₂ surface. Moreover, the disappearance of the peak at 535.0 eV after Pb²⁺ ion adsorption suggests the hydrolysis of ethyl acetate which was previously proposed in Eq. 23. In contrast, the Fe₂O₃/MPTMS sample (Figure 8(e)) showed a decrease in the intensity of the peak at 163.6 eV, associated with the R–SH group, suggesting the formation of a thiolate group with Pb²⁺ ions, i.e., R–S–Pb. In addition, the peak at 168.6 eV shifted toward higher binding energy, likely due to electrostatic interaction between Pb²⁺ ions and the R–SO₃[−] group. However, it appears that the electrostatic interactions are less effective than coordinate/covalent bonding for capturing Pb²⁺ ions which resulted in low Pb²⁺ ion removal efficiency. Furthermore, the overall number of MPTMS molecules reacting with Fe₂O₃ was low, as evidenced by the low sulfur content (Table 4), which in turn indicates low concentration of R–SH groups. Moreover, each MPTMS molecule likely interacts with Fe₂O₃ preferentially via multiple Si–O–Fe linkages, which reduces the number of residual hydroxyl groups on Fe₂O₃ surface available to bind with Pb²⁺ ions via coordinate bonds. These factors account for the low Pb²⁺ ion removal efficiency of Fe₂O₃/MPTMS. As for Fe₂O₃/APTES (Figure 8(f)), the peak attributed to the amino group (R–NH₂) shifted towards higher binding energy, suggesting the formation of covalent bonds with Pb²⁺ ions through the lone pair on the unprotonated amino group or via ion exchange with protons on protonated amino groups.

2.3.2. Effect of Lead Concentration

Given that both Fe₂O₃/TEOS and Fe₂O₃/APTES samples exhibited high and comparable removal efficiencies for Pb²⁺ ions, further studies were conducted to evaluate their performance across different Pb²⁺ ion concentrations. Figures 9(a) and 9(b) present the adsorption capacity and removal efficiency for both samples as a function of Pb²⁺ ion concentration (50–300 ppm) at pH 7. The results show that the adsorption capacity of Fe₂O₃/APTES increased with Pb²⁺ ion concentration, reaching 206 mg/g at 150 ppm, beyond which it plateaued, indicating no further increase. In contrast, the Fe₂O₃/TEOS sample demonstrated a continuous increase in adsorption capacity across the entire concentration range, reaching 519 mg/g at a Pb²⁺ ion concentration of 300 ppm.

The removal efficiency for both samples started high and comparable, above 98%, at 50 ppm. However, as the Pb²⁺ ion concentration increased, the removal efficiency for Fe₂O₃/APTES gradually decreased, reaching about 39% at 300 ppm. This suggests that amine-functionalized IONPs capture Pb²⁺ ions primarily through the amine (NH₂) group, with the surface becoming saturated at 150 ppm, limiting further adsorption beyond this concentration. On the other hand, the Fe₂O₃/TEOS sample demonstrated consistently high removal efficiency across all Pb²⁺ ion concentrations studied, with values fluctuating slightly between 94% and 98%. This superior performance can be attributed to the high porosity of the SiO₂ coating on the Fe₂O₃ surface, which provides a large surface area, enabling the efficient removal of a substantial amount of Pb²⁺ ions. Experimental observations revealed that Pb²⁺ ion solutions with concentrations of 150 ppm and above tend to become turbid, likely due to the precipitation of Pb²⁺ as Pb(OH)₂ at pH 7 (Eq. 26).^[72] We hypothesize that the adsorption of Pb²⁺ ions onto the SiO₂ coating of Fe₂O₃/TEOS nanoparticles promotes the dissolution of Pb(OH)₂ back into the solution by reversing the reaction in Eq. 26, in order to maintain equilibrium according to Le Chatelier's principle.^[74] This equilibrium shift suggests that the SiO₂ coating not only provides a large adsorption surface but also influences the chemical equilibrium of Pb²⁺ ions in the solution, enhancing their removal efficiency.



To gain further insights into the observed behaviour, the adsorption of Pb²⁺ ions on TEOS- and APTES-modified Fe₂O₃

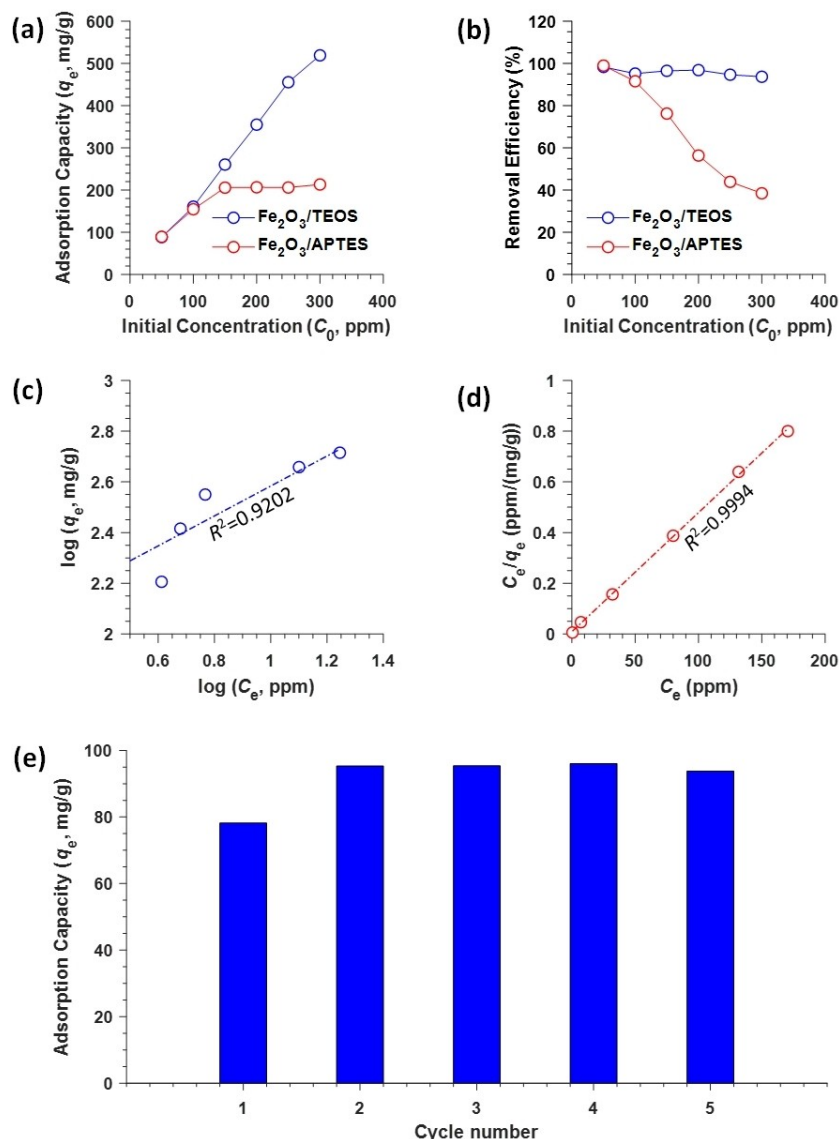


Figure 9. (a) Adsorption capacity (q_e) and (b) removal efficiency calculated for $\text{Fe}_2\text{O}_3/\text{TEOS}$ and $\text{Fe}_2\text{O}_3/\text{APTES}$ as a function of initial Pb^{2+} ion concentration (C_0). Fitting the adsorption behaviour of $\text{Fe}_2\text{O}_3/\text{TEOS}$ and $\text{Fe}_2\text{O}_3/\text{APTES}$ to (c) Freundlich and (d) Langmuir isotherms, respectively, using values of adsorption capacity (q_e) and equilibrium Pb^{2+} ion concentration (C_e). (e) Reusability test of $\text{Fe}_2\text{O}_3/\text{TEOS}$ over 5 cycles of adsorption/desorption of Pb^{2+} ions.

nanoparticles was analyzed using Langmuir and Freundlich adsorption isotherms, which are expressed linearly with Eqs. 27 and 28, respectively.^[2, 4]

$$\text{Langmuir isotherm: } \frac{C_e}{q_e} = \frac{1}{q_{\max} K_L} + \frac{C_e}{q_{\max}} \quad (27)$$

$$\text{Freundlich isotherm: } \log q_e = \log K_F + \frac{1}{n} \log C_e \quad (28)$$

where q_{\max} is the maximum adsorption capacity, K_L and K_F are Langmuir and Freundlich constants, respectively, and $1/n$ is the heterogeneity factor. The adsorption behavior of the $\text{Fe}_2\text{O}_3/\text{TEOS}$ sample was found to align with the Freundlich isotherm, with a regression coefficient (R^2) of 0.9202 (Figure 9(c)), suggesting multilayer adsorption on a heterogeneous surface.

In contrast, $\text{Fe}_2\text{O}_3/\text{APTES}$ exhibited behavior consistent with the Langmuir isotherm, with an R^2 of 0.9994 (Figure 9(d)), indicating monolayer adsorption on a homogeneous surface. This suggests that the TEOS-modified Fe_2O_3 nanoparticles have a more heterogeneous surface with varying affinities for Pb^{2+} ions, allowing for multilayer adsorption. In addition, the $1/n$ value is 0.59, which falls within the range $0 < 1/n < 1$, indicating a favourable adsorption process.^[5] The R^2 value for the $\text{Fe}_2\text{O}_3/\text{TEOS}$ sample in the Freundlich isotherm (0.9202) is relatively lower than expected which might indicate that the adsorption process on this surface is more complex and not perfectly described by the Freundlich model. This complexity may be attributed to the dynamic nature of the system, which involves the dissolution of $\text{Pb}(\text{OH})_2$ and the subsequent adsorption of produced Pb^{2+} ions onto the SiO_2 coating. On the other hand, the APTES-modified Fe_2O_3 nanoparticles provide a more uni-

form surface that facilitates monolayer adsorption of Pb^{2+} ions, exhibiting a maximum adsorption capacity (q_{max}) of 213 mg/g. However, these nanoparticles have fewer active sites for Pb^{2+} ion adsorption compared to the SiO_2 -coated nanoparticles in $\text{Fe}_2\text{O}_3/\text{TEOS}$.

The reusability of the $\text{Fe}_2\text{O}_3/\text{TEOS}$ sample was investigated over 5 cycles of Pb^{2+} ion adsorption and desorption. After each cycle of Pb^{2+} ion adsorption onto $\text{Fe}_2\text{O}_3/\text{SiO}_2$ nanoparticles, nanoparticles were collected and reactivated using a 0.1 M EDTA solution. As shown in Figure 9(e), the initial adsorption capacity of $\text{Fe}_2\text{O}_3/\text{TEOS}$ was calculated to be 78.20 mg/g. Following the desorption of Pb^{2+} ions through chelation with EDTA, the nanoparticle surface was reactivated, resulting in an increased adsorption capacity of 95.32 mg/g in the subsequent adsorption cycle, exceeding the initial value. This improvement in adsorption capacity may be attributed to the enrichment of the SiO_2 coating with hydroxyl groups in the acidic EDTA solution (pH 4.7). Over subsequent cycles, the material consistently demonstrated high adsorption capacity, with a slight decrease observed by the fifth cycle, reaching 93.81 mg/g. These results highlight the efficacy of $\text{Fe}_2\text{O}_3/\text{TEOS}$ as a reusable material for Pb^{2+} ion removal.

As shown above, $\text{Fe}_2\text{O}_3/\text{TEOS}$ demonstrates high effectiveness for the magnetic removal of Pb^{2+} ions from aqueous systems. This is due to its $\text{Fe}_2\text{O}_3/\text{SiO}_2$ core-shell structure, which offers superior performance compared to other magnetic adsorbents as summarized in Table S3. With an impressive adsorption capacity of 519 mg/g, $\text{Fe}_2\text{O}_3/\text{TEOS}$ surpasses other materials, including Fe_3O_4 -based composites and functionalized nanoparticles, along with a removal efficiency of 94%. While some magnetic adsorbents approach 100% removal efficiency, they tend to have lower adsorption capacities than $\text{Fe}_2\text{O}_3/\text{TEOS}$. In addition, $\text{Fe}_2\text{O}_3/\text{TEOS}$ maintains its high efficiency even with short contact time (30 min) and high initial Pb^{2+} concentration (up to 300 ppm). This exceptional performance is largely attributed to the small size of $\text{Fe}_2\text{O}_3/\text{SiO}_2$ nanoparticles which enables a high surface area-to-volume ratio, and the presence of the SiO_2 coating itself which appears porous providing a significant surface area for Pb^{2+} ion adsorption. This positions $\text{Fe}_2\text{O}_3/\text{TEOS}$ as a highly promising material for heavy metal remediation applications.

3. Conclusions

This study presents a novel electrochemical approach for synthesizing iron oxide nanoparticles (IONPs) at various voltages, followed by their electrochemical silanization. The modified IONPs were then evaluated for the magnetic removal of lead (Pb^{2+}) ions from aqueous solutions. The key findings are summarized as follows:

- 1 *Influence of synthesis voltage:* The properties of IONPs are significantly influenced by the applied synthesis voltage. Higher voltages increase the electrolyte temperature, leading to enhanced yield, crystallinity, and magnetic properties. These improvements are attributed to the electrothermal annealing induced by the Joule heating effect. The optimal

IONPs were synthesized at 40 V, primarily in the maghemite phase ($\gamma\text{-Fe}_2\text{O}_3$), which were subsequently silanized.

- 2 *Electrochemical silanization:* The study successfully demonstrated the electrochemical silanization of Fe_2O_3 nanoparticles using TEOS, MPTMS, and APTES. TEOS modification resulted in the formation of a thick SiO_2 coating, producing a core-shell structure ($\text{Fe}_2\text{O}_3/\text{SiO}_2$). In contrast, MPTMS and APTES formed thinner layers, functionalizing Fe_2O_3 surface with thiol (SH) and amine (NH_2) groups, respectively. However, the partial oxidation of the thiol group was observed, likely due to its electrooxidation or due to the elevated temperature during the electrosilanization process.
- 3 *Efficiency in Pb^{2+} ion removal:* The silane-modified Fe_2O_3 nanoparticles were evaluated for their ability to magnetically remove Pb^{2+} ions from aqueous solutions. Among the silane-modified Fe_2O_3 samples, $\text{Fe}_2\text{O}_3/\text{TEOS}$ exhibited superior performance, with a high adsorption capacity of 519 mg/g and consistently high removal efficiency across various Pb^{2+} ion concentrations. In addition, this material proved to be reusable over multiple cycles of Pb^{2+} ion adsorption and desorption. This exceptional performance is attributed to the $\text{Fe}_2\text{O}_3/\text{SiO}_2$ core-shell structure and the high surface area-to-volume ratio of these nanoparticles.

Experimental Section

Materials and Reagents

Iron rod (99.99%) was purchased from Goodfellow (UK), while Pt coil and graphite rod were obtained from MSE Supplies (USA), all electrodes with a 6 mm diameter. Ethanol (undistilled, 100%), NaCl and ethylenediaminetetraacetic acid disodium salt (EDTA) were sourced from ChemSupply (Australia). Sodium dodecyl sulfate (SDS, ultrapure) was purchased from Applichem (Germany). Tetraethoxysilane (TEOS, reagent grade), (3-mercaptopropyl)trimethoxysilane (MPTMS, 95%), (3-aminopropyl)triethoxysilane (APTES, 99%), Lead (Pb) standard solution (1000 ppm in 2% HNO_3 , AAS grade), and LiCl were provided by Sigma-Aldrich (Australia). HNO_3 (70%) was supplied by Ajax FineChem (Rowe Scientific, Australia). HCl (32%) was purchased from RCI Labscan Limited (Thailand). Deionized water (resistivity of 18 $\text{M}\Omega\cdot\text{cm}$) was obtained from a PURELAB[®] Quest system. All chemicals and solvents were used without any further purification or treatment.

Electrosynthesis of Nanoparticles

Iron oxide nanoparticles (IONPs) were electrochemically synthesized in a 50-mL Redox.me electrochemical cell using a Pt coil as the cathode and an iron rod as the anode. The electrodes were positioned 0.5 cm apart, with 2 cm of the iron rod immersed in the electrolyte. The electrolyte consisted of 50 mM LiCl and 50 mM SDS prepared in ethanol (with 5% water). Prior to electrosynthesis, the iron rod was cleaned by sonication in 1 M HCl for 10 min, followed by rinsing with deionized water

then ethanol. The electrosynthesis process was conducted potentiostatically under stirring (300 rpm) in 25 mL of electrolyte at various voltages (10–40 V) for 30 min, using a Major Science MP-300 V power supply. The response current and electrolyte temperature were monitored over time. The resulting IONPs were collected and washed three times with ethanol *via* centrifugation at 2000 rpm for up to 4 min. After washing, the IONPs were either dried under vacuum at 60 °C for 1 h or resuspended in 25 mL of ethanol by vortexing and bath sonication for 10 min. The resuspended samples were then stored at 4 °C. The final concentrations of the IONP suspensions were 1.0, 4.0, 7.5, and 10.0 mg/mL for nanoparticles synthesized at 10, 20, 30, and 40 V, respectively.

Electrosilanization of Nanoparticles

The IONPs synthesized at 40 V exhibited the highest crystallinity and enhanced magnetic properties, so they were selected for subsequent modification with silane reagents. Silanization of IONPs was performed using a 25 mL mixed solution containing 50 mM silane reagent (TEOS, MPTMS, or APTES) and 50 mM LiCl in ethanol (with 5% water). Prior to this process, 5 mL of the IONP/ethanol suspension (10 mg/mL) was exposed to an external neodymium (Nd) magnet (AMF Magnetics) to collect the IONPs. The collected IONPs were then resuspended in the silanization electrolyte by vortexing and bath sonication for 10 min. The silanization process was carried out under vigorous stirring (1500 rpm) at a voltage of 40 V for 30 min, with continuous monitoring of current and temperature. The silane-modified IONPs were collected and rinsed three times by magnetic decantation to remove any silica particles formed through self-condensation. Finally, they were resuspended in 5 mL of ethanol, vortexed and bath sonicated for 10 min, and stored at 4 °C.

Characterization Techniques

Powder X-ray diffraction (XRD) analysis was conducted to investigate the crystallinity of the IONPs electrosynthesized at different voltages. Samples for XRD analysis were prepared by concentrating an amount of IONP suspension equivalent to 10 mg by centrifugation at 4,400 rpm for up to 4 min, followed by re-suspension in 200 μ L ethanol. The concentrated suspension was then cast onto a film of carbon tape mounted on a 1 cm² piece of microscope glass slide. The samples were then dried at 60 °C under vacuum for 1 h. XRD patterns were collected using a Bruker D2 PHASER X-ray diffractometer with a cobalt (Co) source, $K\alpha_1$ wavelength of 1.78897 Å, over a 2θ range of 10–90° with a step size of 0.03° and time per step of 1 s. The samples were rotated during measurement at a speed of 15°/min. The same procedure was used to collect the XRD pattern for carbon tape alone (without IONPs), which was then subtracted from the XRD patterns of IONPs to eliminate the carbon tape contribution. For comparison with standard diffraction patterns, the XRD data were converted to Cu-

irradiated form using the Cu $K\alpha_1$ wavelength of 1.54056 Å^[75] using Eq. 29 derived from Bragg's formula $n\lambda = 2d\sin\theta$,^[76] where n is the order of reflection, λ is the wavelength of the X-ray, d is the interplanar spacing, and θ is the angle of X-ray incidence, given that the d value is independent of the irradiation source. On the other hand, the crystallite size (D) was calculated *via* the Sherrer equation,^[13] $D = K\lambda/\beta\cos\theta$, where K is the shape factor (0.9), and β is the full width at half maximum (FWHM) of the diffraction peak.

$$\sin\theta_{\text{Cu}} = \sin\theta_{\text{Co}} \times \frac{\lambda_{\text{Cu}}}{\lambda_{\text{Co}}} \quad (29)$$

The chemical structure of the IONPs before and after silanization were investigated using transmission Fourier transform infrared (FTIR) spectroscopy. A 20 μ L aliquot of each nanoparticle suspension was mixed with approximately 100 mg of potassium bromide (KBr) and dried at 60 °C under vacuum for 1 h. The dried KBr/nanoparticle mixture was then ground with a mortar and pestle, then pressed using a hydraulic machine at 10 tons to make pellets. The obtained pellets were analyzed using a ThermoFisher Nicolet iS5 FT-IR spectrometer, operated with OMNIC software, by collecting 64 scans at a resolution of 2 cm⁻¹.

The magnetic properties of the IONPs synthesized, at different voltages, were studied at 300 K using a Quantum Design MPMS3 Superconducting Quantum Interference Device (SQUID) magnetometer. The measurements were conducted in vibrating sample magnetometry (VSM) mode, scanning from 2 T to -2 T with an average sweep rate of 10 Oe/s using dry powder samples with an approximate mass of 5 mg. The raw data were converted to magnetic moment per unit mass (in emu/g) for comparison between samples.

The morphology of the pristine and modified IONPs was observed using transmission electron microscopy (TEM). Low-resolution TEM images were obtained using a Tecnai T12 operating at 120 kV. High-resolution (HR) TEM images were collected using a ThermoFisher Themis Z aberration-corrected TEM at an accelerating voltage of 300 kV. Particle size distribution and d-spacings were analyzed from HR-TEM images using ImageJ 1.54 g software.

X-ray photoelectron spectroscopy (XPS) was performed to analyze the elemental composition and valence states of surface atoms in both pristine and silane-modified samples. XPS spectra were acquired using a Kratos Axis Supra Plus instrument equipped with a monochromatic Al $K\alpha$ X-ray source (1486.6 eV) operating at 100 W (10 kV, 10 mA). Samples were scanned at a pass energy of 160 eV over a binding energy range of 0–1200 eV, with 1.0 eV steps and a scan time of 120 s. Narrow high-resolution (HR) scans were conducted at a pass energy of 20 eV, with 0.1 eV steps and a scan time of 60 s, allowing up to 3 sweeps per HR scan. During sample analysis, the base pressure in the analysis chamber was maintained below 10⁻⁸ Torr. Each sample was prepared by drop-casting 20 μ L of nanoparticle suspensions onto a 1 cm² piece of a Si wafer, which was then dried under vacuum at 60 °C for 1 h. XPS data were processed using CasaXPS software (version 2.3.18), with all

spectra calibrated to the binding energy of 284.8 eV, corresponding to adventitious carbon. A residual standard deviation (STD) of ≤ 1.0 was considered indicative of a good fit between the fitted and experimental XPS data. XPS-based atomic compositions were determined from three spots per sample, with the average value reported along with the STD.

The surface charge of pristine and silane-modified IONPs was measured using zeta potential analysis. All measurements were performed using a Malvern Zetasizer Ultra. A 100 μL aliquot of each sample suspension was diluted to 10 mL with 10 mM NaCl (pH 7). The resulting suspension was then probe sonicated at a power of ~ 35 W for 30 seconds, followed by bath sonication for 5 min. Zeta potential measurements were conducted at room temperature in three runs per sample after being pre-equilibrated for 120 s, and a control sample was prepared using unmodified IONPs.

Adsorption Experiments for Lead Ion Removal

Pristine (unmodified) and TEOS-, MPTMS-, and APTES-modified IONPs were used for the magnetic removal of Pb^{2+} ions from their aqueous solutions. For each experiment, a suitable amount of nanoparticle suspension (equivalent to 5 mg nanoparticles) was placed in a 50-mL tube and exposed to a Nd magnet to collect the nanoparticles. Then, the nanoparticles were resuspended in 10 mL of Pb^{2+} ion solution, with the studied concentration, and the pH was adjusted to 7. The Pb^{2+} ion/nanoparticle suspension was vortexed, followed by shake incubation at room temperature at a speed of 200 rpm for 30 min. Afterwards, the nanoparticles were collected by magnetic decantation, and a portion of the supernatant was diluted to 10 mL using 2% HNO_3 with a dilution factor of 1/60 to determine the concentration of the residual Pb^{2+} ions. This was conducted *via* inductively coupled plasma-optical emission spectroscopy (ICP-OES) using a Thermo Scientific iCAP 7000 Series ICP spectrometer operated with Qtegra ISDS Software. Each material was tested in 50 ppm Pb^{2+} ion solution twice, using two independently synthesized samples per material. TEOS- and APTES-modified IONPs demonstrated the highest Pb^{2+} ion removal efficiency, so their Pb^{2+} ion removal capabilities were further investigated in solutions with higher Pb^{2+} ion concentrations, i.e., 100, 150, 200, 250, and 300 ppm.

To understand the Pb^{2+} ion removal mechanism using pristine and silane-modified IONPs, *ex-situ* (post-treatment) XPS analysis was conducted to investigate the interactions between Pb^{2+} ions and the surface-functional groups of pristine, TEOS-, MPTMS-, and APTES-modified IONPs. Samples were prepared by collecting the nanoparticles from Pb^{2+} ion solutions, washing them three times with 5 mL of deionized water, and then resuspending them in 0.5 mL of de-ionized water. Subsequently, 20 μL of each suspension was drop cast onto a piece of Si wafer and left to dry at 60 $^\circ\text{C}$ for 12 h.

The reusability of TEOS-modified IONPs was evaluated through five cycles of Pb^{2+} ion adsorption/desorption. In each cycle, 5 mg of nanoparticles, pre-treated in 10 mL of 50 ppm Pb^{2+} solution, were reactivated by vortexing and shake-

incubation in 10 mL of 0.1 M EDTA (pH 4.7) for 15 minutes, followed by two rinses with water. The activated nanoparticles were then resuspended in 10 mL of fresh 50 ppm Pb^{2+} solution for the next adsorption cycle.

Supporting Information

The authors have cited additional references within the Supporting Information.^[1–2, 7, 15, 77–79]

Acknowledgments

We acknowledge the US-Australia International Multidisciplinary University Research Initiative (AUSMURI) Scheme for funding (Grant Number: AUSMURIV000001). This work was performed in part at the Trace Analysis for Chemical, Earth and Environmental Sciences (TrACEES) Platform at the University of Melbourne. We also acknowledge the Australian Research Council for an equipment grant (LE210100009). Open Access publishing facilitated by Swinburne University of Technology, as part of the Wiley - Swinburne University of Technology agreement via the Council of Australian University Librarians. Open Access publishing facilitated by Swinburne University of Technology, as part of the Wiley - Swinburne University of Technology agreement via the Council of Australian University Librarians.

Conflict of Interests

The authors declare no conflict of interest.

Data Availability Statement

The data that support the findings of this study are available from the corresponding author upon reasonable request.

Keywords: Nanoparticles • Electrodeposition • Surface modification • Silanes • Magnetic lead removal

- [1] D. Patino-Ruiz, L. Rehmann, M. Mehrvar, E. Quinones-Bolanos, A. Herrera, *RSC Adv.* **2020**, *10*, 39284–39294.
- [2] M. A. Habila, M. S. Moshab, A. M. El-Toni, A. S. Al-Awadi, Z. A. AlOthman, *ACS Omega* **2023**, *8*, 7626–7638.
- [3] A. Gallo-Cordova, M. d P Morales, E. Mazarío, *Water* **2019**, *11*, 2372.
- [4] A. U. Rehman, U. Sharafat, S. Gul, M. A. Khan, S. B. Khan, M. Ismail, M. I. Khan, *Green Process. Synth.* **2022**, *11*, 287–305.
- [5] A. A. Pawar, R. Kumar, S. Sharma, T. Satyanarayana, *Part. Part. Syst. Charact.* **2022**, *39*, 2200156.
- [6] M. Yaseen, A. Khan, M. Humayun, S. Farooq, N. Shah, S. Bibi, Z. A. K. Khattak, A. U. Rehman, S. Ahmad, S. M. Ahmad, M. Bououdina, H. Ullah, *Macromol. Mater. Eng.* **2023**, *308*, 2200695.
- [7] Y. Huang, A. A. Keller, *Water Res.* **2015**, *80*, 159–168.
- [8] F. Tu, Y. Yu, Y. Wang, L. Huang, D. Ye, Z. Fu, *Ceram. Int.* **2024**, *50*, 2976–2986.
- [9] B. E. Keshta, A. H. Gemeay, D. Kumar Sinha, S. Elsharkawy, F. Hassan, N. Rai, C. Arora, *Results Chem.* **2024**, *7*, 101388.

- [10] K. Gandha, J. Mohapatra, M. K. Hossain, K. Elkins, N. Poudyal, K. Rajeshwar, J. P. Liu, *RSC Adv.* **2016**, *6*, 90537–90546.
- [11] S. P. Schwaminger, P. Fraga-García, F. Selbach, F. G. Hein, E. C. Fuß, R. Surya, H.-C. Roth, S. A. Blank-Shim, F. E. Wagner, S. Heissler, S. Berensmeier, *Adsorption* **2016**, *23*, 281–292.
- [12] M. Starowicz, P. Starowicz, J. Zukrowski, J. Przewoznik, A. Lemanski, C. Kapusta, J. Banas, *J. Nanopart. Res.* **2011**, *13*, 7167–7176.
- [13] A. Ahmadi, *Anal. Bioanal. Chem.* **2019**, *11*, 625–634.
- [14] D. Cao, H. Li, L. Pan, J. Li, X. Wang, P. Jing, X. Cheng, W. Wang, J. Wang, Q. Liu, *Sci. Rep.* **2016**, *6*, 32360.
- [15] S. Villa, P. Riani, F. Soggia, E. Magi, F. Canepa, *J. Nanopart. Res.* **2019**, *21*, 21–44.
- [16] F. Ahangaran, A. H. Navarchian, *Adv. Colloid Interface Sci.* **2020**, *286*, 102298.
- [17] B. K. Sodipo, A. A. Aziz, *J. Magn. Magn. Mater.* **2016**, *416*, 275–291.
- [18] V. C. Karade, A. Sharma, R. P. Dhavale, R. P. Dhavale, S. R. Shingte, P. S. Patil, J. H. Kim, D. R. T. Zahn, A. D. Chougale, G. Salvan, P. B. Patil, *Sci. Rep.* **2021**, *11*, 5674.
- [19] A. A. Issa, A. S. Luyt, *Polymers (Basel)*. **2019**, *11*, 537.
- [20] D. Ramimoghaddam, S. Bagheri, S. B. A. Hamid, *J. Magn. Magn. Mater.* **2014**, *368*, 207–229.
- [21] J. Li, L. Luo, S. Wang, H. Song, B. Jiang, *PhotoMat* **2024**, 1–37. DOI: 10.1002/phmt.14.
- [22] H. B. Lee, G. K. Veerasubramani, K. S. Lee, H. Lee, T. H. Han, *Carbon* **2022**, *198*, 252–263.
- [23] E. V. Shkol'nikov, *Russ. J. Appl. Chem.* **2011**, *84*, 1702–1709.
- [24] X. Xuan, D. Li, *J. Chromatogr. A* **2005**, *1064*, 227–237.
- [25] C. C. Wu, H. Y. Yen, L. T. Lai, G. C. Perng, C. R. Lee, S. J. Wu, *Sensors (Basel)* **2020**, *20*, 3728.
- [26] N. Kaihovirta, A. Asadpoordarvish, A. Sandstrom, L. Edman, *ACS Photonics* **2014**, *1*, 182–189.
- [27] M. Kubota, T. Yokoi, T. Ogawa, S. Saito, M. Furuya, K. Yokota, H. Kanetaka, B. Jayadevan, M. Kawashita, *Ceram. Int.* **2021**, *47*, 12292–12299.
- [28] Y. Chen, S. Sun, Y. Lai, C. Ma, *Appl. Therm. Eng.* **2016**, *100*, 340–347.
- [29] E. C. Fuchs, A. D. Wexler, L. L. F. Agostinho, M. Ramek, J. Woisetschlager, *J. Phys. Conf. Ser.* **2011**, *329*, 012003.
- [30] H. Hongwen, X. Guangchen, G. Fu, *J. Semicond.* **2009**, *30*, 033006.
- [31] O. L. Gribkova, A. A. Nekrasov, *Polymers (Basel)*. **2022**, *14*, 3201.
- [32] J. Steeb, M. Josowicz, J. Janata, *Anal. Chem.* **2009**, *81*, 1976–1981.
- [33] H. Rasouli, M. G. Hosseini, H. Mashhady Kashtiban, *Mater. Chem. Phys.* **2021**, *272*, 124953.
- [34] H. Mashhadi kashtiban, H. Rasouli, P. Y. Sefidi, M. G. Hosseini, *Mater. Sci. Semicond. Process.* **2022**, *141*, 106425.
- [35] J. Winsett, A. Moilanen, K. Paudel, S. Kamali, K. Ding, W. Cribb, D. Seifu, S. Neupane, *SN Appl. Sci.* **2019**, *1*, 1–8.
- [36] F. Mohammadi, S. Amiri, E. Mirzaei, A. Gholami, P. D. Cozzoli, *J. Nanomater.* **2022**, *2022*, 7012012.
- [37] L. Kuang, Y. Liu, D. Fu, Y. Zhao, *J. Colloid Interface Sci.* **2017**, *490*, 259–269.
- [38] P. A. Connor, K. D. Dobson, A. J. & McQuillan, *Langmuir* **1999**, *15*, 2402–2408.
- [39] Y. Masubuchi, Y. Sato, A. Sawada, T. Motohashi, H. Kiyono, S. Kikkawa, *J. Eur. Ceram. Soc.* **2011**, *31*, 2459–2462.
- [40] S. F. Wang, Q. Li, X. T. Zu, X. Xiang, W. Liu, S. Li, *J. Magn. Magn. Mater.* **2016**, *419*, 464–475.
- [41] J. C. Picuri, J. M. Natoli, S. E. Shaw, S. P. Shyam, S. R. VanHoesen, Z. Lin, W. J. Bowyer, *Colorants* **2022**, *1*, 363–375.
- [42] G. Casula, M. Fantauzzi, B. Elsener, A. Rossi, *Coating* **2024**, *14*, 327.
- [43] K. Fukushima, S. Y. Lee, K. Tanaka, K. Sasaki, T. Ishizaki, *Materials (Basel)* **2022**, *15*, 3270.
- [44] M. L. Chelaghmia, M. Nacef, H. Fisli, A. M. Affoune, M. Pontie, A. Makhlof, T. Derabla, O. Khelifi, F. Aissat, *RSC Adv.* **2020**, *10*, 36941–36948.
- [45] J. R. N. Santos, D. S. S. Viégas, I. C. B. Alves, A. D. Rabelo, W. M. Costa, E. P. Marques, L. Zhang, J. Zhang, A. L. B. Marques, *Electrocatalysis* **2019**, *10*, 560–572.
- [46] A. Meng, H. Zhang, B. Huangfu, W. Tian, L. Sheng, Z. Li, S. Tan, Q. Li, *Prog. Nat. Sci.* **2020**, *30*, 461–468.
- [47] T. Girardet, P. Venturini, H. Martinez, J.-C. Dupin, F. Cleymand, S. Fleutot, *Appl. Sci.* **2022**, *12*, 8127.
- [48] P. A. Connor, K. D. Dobson, A. J. & McQuillan, *Langmuir* **1999**, *15*, 2402–2408.
- [49] A. C. Boden, M. Bhave, L. Cipolla, P. Kingshott, *Appl. Surf. Sci.* **2022**, *602*, 154282.
- [50] M.-C. Brochier Salon, M. N. Belgacem, *Phosphorus Sulfur Silicon Relat. Elem.* **2011**, *186*, 240–254.
- [51] R. Bel-Hassen, S. Boufi, M. C. B. Salon, M. Abdelmouleh, M. N. Belgacem, *J. Appl. Polym. Sci.* **2008**, *108*, 1958–1968.
- [52] S. Savard, L.-P. Blanchard, J. Léonard, R. E. Prud'homme, *Polym. Compos.* **1984**, *5*, 242–249.
- [53] M. Pantoja, F. Velasco, D. Broekema, J. Abenojar, J. C. d Real, *J. Adhes. Sci. Technol.* **2010**, *24*, 1131–1143.
- [54] V. V. Annenkov, E. N. Danilovtseva, V. A. Pal'shin, O. G. N. Verkhozina, S. N. Zelinskiy, U. M. Krishnan, *RSC Adv.* **2017**, *7*, 20995–21027.
- [55] M.-C. Brochier Salon, P.-A. Bayle, M. Abdelmouleh, S. Boufi, M. N. Belgacem, *Colloids Surf. A* **2008**, *312*, 83–91.
- [56] J. P. Cloarec, C. Chevalier, J. Genest, J. Beauvais, H. Chamas, Y. Chevolot, T. Baron, A. Souifi, *Nanotechnology* **2016**, *27*, 295602.
- [57] L. Jayarathna, A. Bandara, W. J. Ng, R. Weerasooriya, *J. Environ Health Sci Eng* **2015**, *13*, 54.
- [58] C. Yao, J. Yu, Y. Wang, C. Tang, C. Huang, *Dent. Mater.* **2018**, *34*, 809–818.
- [59] M. Rostami, M. Mohseni, Z. Ranjbar, *Pigm. Resin Technol.* **2011**, *40*, 363–373.
- [60] J. Zhang, P. Zhang, F. Cheng, *Minerals* **2022**, *12*, 705.
- [61] S.-Y. Jing, Heon-Ju Lee, C. K. Choi, *J. Korean Phys. Soc.* **2002**, *41*, 769–773.
- [62] B. Lai, F. Mei, Y. Gu, *Chem. Asian J.* **2018**, *13*, 2529–2542.
- [63] Y. Liu, S. Zhang, Y. He, C. Chen, C. Zhang, P. Xie, F. Zhong, H. Li, J. Chen, Z. Li, *Coating* **2021**, *11*, 178.
- [64] M. E. Simonsen, C. Sønderby, Z. Li, E. G. Søgaaard, *J. Mater. Sci.* **2009**, *44*, 2079–2088.
- [65] H. Tissot, L. Li, S. Shaikhutdinov, H. J. Freund, *Phys. Chem. Chem. Phys.* **2016**, *18*, 25027–25035.
- [66] R. Włodarczyk, J. Sauer, X. Yu, J. A. Boscoboinik, B. Yang, S. Shaikhutdinov, H. J. Freund, *J. Am. Chem. Soc.* **2013**, *135*, 19222–19228.
- [67] Y. L. Khung, S. H. Ngalm, A. Scaccabarozzi, D. Narducci, *Beilstein J. Nanotechnol.* **2015**, *6*, 19–26.
- [68] X. Rao, M. Tatoulian, C. Guyon, S. Ognier, C. Chu, A. Abou Hassan, *Nanomaterials* **2019**, *9*, 1034.
- [69] A. B. Shatan, K. Venclikova, B. A. Zasonska, V. Patsula, O. Pop-Georgievski, E. Petrovsky, D. Horak, *Pharm. Res.* **2019**, *36*, 147.
- [70] S. S. Kim, L. Britcher, S. Kumar, H. J. Griesser, *Sains Malays.* **2018**, *47*, 1913–1922.
- [71] G. Ambrozic, M. Kolypadi Markovic, R. Peter, I. Kavre Piltaver, I. Jelovica Badovinac, D. Cakara, D. Markovic, M. Knez, *J. Colloid Interface Sci.* **2020**, *560*, 303–311.
- [72] Y. Zhou, S. Xia, J. Zhang, B. T. Nguyen, Z. Zhang, *Chem. Eng. J.* **2017**, *308*, 1098–1104.
- [73] K. N. Dalby, H. W. Nesbitt, V. P. Zakaznova-Herzog, P. L. King, *Geochim. Cosmochim. Acta* **2007**, *71*, 4297–4313.
- [74] J. Zhu, L. Li, M. Cao, *Nano Energy* **2024**, *122*, 109300.
- [75] G. Perenlei, P. C. Talbot, W. N. Martens, J. Riches, J. A. Alarco, *RSC Adv.* **2017**, *7*, 15632–15643.
- [76] F. Tavakoli, M. Mamaghani, M. Sheykhan, *Appl. Organomet. Chem.* **2019**, *33*, e5083.
- [77] J. Feng, J. Zhang, W. Song, J. Liu, Z. Hu, B. Bao, *Ecotoxicol. Environ. Saf.* **2020**, *203*, 111002.
- [78] P. K. Gautam, S. Shivalkar, S. Banerjee, *J. Mol. Liq.* **2020**, *305*, 112811.
- [79] C. Zou, W. Jiang, J. Liang, X. Sun, Y. Guan, *Environ. Sci. Pollut. Res. Int.* **2019**, *26*, 1315–1322.

Manuscript received: September 28, 2024
Revised manuscript received: December 25, 2024
Accepted manuscript online: January 17, 2025
Version of record online: February 4, 2025